CIRM 17
August 1998

NATIONAL PHYSICAL LABORATORY

Neutron scatter characteristics of the low-scatter facility of the Chadwick Building, NPL

by

G.C. Taylor and D.J. Thomas
Centre for Ionising Radiation Metrology

Abstract

The aim of this work was to provide information which could be used to improve the efficiency and cost effectiveness with which regular calibrations and checks of area survey instruments and personal dosemeters are carried out. To this end the variation in fractional scatter component with distance from the neutron source has been determined using calculation, spectrometry and by reviewing the results of calibrations carried out since 1989, together with studies performed at NPl in 1982 and 1988. Scatter fraction relationships have been produced for ^{241}Am-Be and ^{252}Cf sources, in terms of neutron fluence, ambient dose equivalent and instrument responses.

© Crown copyright 1998
Reproduced by permission of the Controller of HMSO

ISSN 1369-6793

National Physical Laboratory
Teddington, Middlesex, UK, TW11 0LW

Extracts from this report may be reproduced
provided the source is acknowledged

Approved on behalf of Managing Director NPL, by Dr Julian Hunt
Head, Centre for Ionising Radiation Metrology.

CONTENTS

1. INTRODUCTION

1.1 Dosemeter Calibrations and Neutron Scatter

The standard procedure for calibrating a neutron-sensitive detector involves the use of a neutron source of known spectrum and known emission rate positioned at a known distance from the instrument. A *fluence response*[1], or more precisely a *fluence response characteristic*[2], may then be calculated for the instrument by dividing the detector reading by the neutron fluence calculated at the *effective centre* of the device. The fluence at the device is derived by assuming an inverse-square law dependence with distance from the source. More commonly, the response is determined in terms of the quantity *dose equivalent*, which involves the extra step of multiplying the fluence by the *fluence to dose equivalent conversion factor* for the particular source used. The inverse of the fluence or dose equivalent responses are the fluence and dose equivalent *calibration factors*[1].

Unfortunately, the calibration process is rarely as straightforward as it first appears, and this is due, in the main, to *neutron scatter*. Incident neutrons from the source can be scattered, by the air, away from a path that impinges on the detector; conversely, neutrons that would not have impinged on the detector may be scattered towards it by the air, by other fixtures in the irradiation room, e.g. source and detector stands, or by the walls, floor or ceiling of the room.

The problem with scatter is that it effectively alters the fluence and spectrum of the neutrons incident on the detector, invalidating the standard calibration procedure outlined above. As a result, any calibration performed must be corrected to eliminate any contribution to the fluence response from the scattered neutrons, leaving a value derived solely from those incident directly from the source. This 'uncontaminated' value is termed the *free field (fluence) response* and, because it has been determined for those neutrons coming from the source alone, its value should be independent of the calibration facility; hence it should be reproducible by any calibration facility using the same neutron source.

The degree to which neutron scatter affects a specific device's calibration factor is influenced by three parameters: the magnitude of the scattered fluence, the device's energy response, and the scatter spectrum. As a result, no two designs of device will respond in quite the same way, which means no single scatter correction factor will be applicable.

1.2 Calibration Facilities at NPL

Most neutron irradiations at the National Physical Laboratory are performed in the low-scatter facility (or Main Bay) of the Chadwick Building (Bldg 47). This is an enormous room: 23 metres long, 17 metres wide and 18 metres high, with thick (~1 metre) concrete shielding walls. The roof, however, is comparatively thin, being ~25 cm thick concrete. Irradiations are predominantly performed towards one end of the room where the source is mounted 7 m from the nearest walls and above a pit whose floor is roughly 6 m below the source. Adjustments to the source stand are facilitated by a circular platform, known as the pit circle, roughly 1.5 m below the source position. The detectors are typically mounted on stands attached to small carriages on rotatable arms pivoted about a point below the source position. All movement of the carriages and arms is controlled remotely. The detector positions and the pit circle are accessed via low density, movable walkways.

Routine calibrations are performed using either ^{241}Am-Be (α,n) or ^{252}Cf (spontaneous fission) sources, encapsulated in stainless steel. Both are fast neutron sources, with mean energies of 4.2 and 2.1 MeV respectively. Other sources available, but used much less frequently, are ^{241}Am-F, ^{241}Am-Li, ^{241}Am-b and heavy water moderated ^{252}Cf. The facility is also used for performing calibrations with accelerator-produced monoenergetic neutrons.

1.3 Techniques for Determining Neutron Scatter

Measurements of neutron scatter are not always easy to perform, and those that are can be of limited value. If calibrations are always performed at a specific distance for a specific design of dosemeter, then a straightforward scatter measurement using the *shadow cone technique* may be performed, and the *scatter fraction* obtained in this way used in all subsequent calibrations for this type of dosemeter (provided that no changes are made to the measurement conditions).

The shadow cone technique is an intuitively obvious experimental approach to determining a neutron scatter component. Essentially, it involves blocking the path between the neutron source and the dosemeter so that no neutrons can reach the device directly from the source. The shadow cones constructed at NPL conform to the recommendations laid out in the ISO Standard 10647[1]. These consist of two parts, a 20 cm long front portion made of iron, and a 30 cm long rear section made of boron-loaded polyethylene or paraffin wax. This configuration has a negligible transmission factor for neutrons emitted by ^{241}Am-Be and ^{252}Cf sources. Ideally, the cone is positioned between the source and the detector in such a way that they fall within the areas defined by extrapolating the cone beyond the narrow and the wide ends respectively, but without excessive overshadowing, as shown in Figure 1. It is also important that neither the source nor the detector are positioned too close to the cone, otherwise this may interfere with the creation and detection of the scattered neutron field which would be present in the absence of the cone. A measurement performed under these conditions will yield a response for the scatter-only neutron field, which may then be subtracted from the total response, thus determining the free field response and hence the calibration factor for the direct-only neutron field.

If, however, several calibrations are needed at a variety of source-detector distances, the equivalent number of scatter measurements are needed. This may be time-consuming and therefore expensive.

In situations where it is impractical to use a shadow cone, either the semi-empirical or the generalised fit methods may be used. Both approaches rely on determining the <u>total</u> fluence response (including scattered neutrons) at a series of distances from the source, from which the free field response can be derived by fitting the data to a polynomial of up to second order in the distance.

With the semi-empirical method, the response to room-scattered neutrons is assumed to be constant at all measurement locations and the air-scatter component is assumed to fall linearly with distance. A linear fit to the data in terms of (distance)^2 yields the free field fluence response from the intercept term, and the product of the response and the fractional room scatter component at 1 m source-detector distance, from the gradient term.

The coefficients of the generalised fit method have no physical meaning, but the method is more widely applicable and has fewer limitations. A more detailed discussion of these techniques and their limitations my be found in ISO 10647[1].

Neutron scatter is, however, amenable to calculation. In recent years computer programs termed *Monte Carlo transport codes* have become more widely available, due in no small part to the continuing decrease in cost and increasing power of personal computers. Their use does, however, require a detailed knowledge of the irradiation facility in terms of configuration, content and composition.

A third approach is to predict the scatter contribution by analytical means, using a generalised model of the calibration facility[3]. However, this approach is beyond the scope of this report.

One final method is to measure the neutron spectrum at a range of calibration positions. This has the advantage of being independent of the instrument being calibrated, although it does rely on accurate knowledge of the instrument's energy response characteristics. Furthermore, the only spectrometer capable of measuring the entire range of neutron energies, from below thermal to a few MeV, is a Bonner sphere set. Such a measurement entails measuring the count rate in a thermal neutron detector inside eight or more different diameter moderating spheres, behind a suitable shadow cone, for every calibration position for which the neutron spectrum is desired. Furthermore, because the scatter fraction is small, the counting rate is likely to be low, hence long counting times will be required in order to achieve the necessary statistical precision. This makes the measurements time-consuming and therefore expensive.

The optimum approach to determining the scatter characteristics of a facility lies in a combination of experiment and calculation, where the experimental results can be used to validate the calculations.

2. PREVIOUS RESULTS

Previous work by NPL in this area has been published in an NPL report CIRA(EXT)004[4], which concentrated on the modelling of the low scatter area (Main Bay) for irradiation distances of 75 cm and 150 cm using the transport code MCNP[5]. A comparison between the predicted fluence 150 cm from a ^{252}Cf source agreed with the equivalent Bonner sphere measurement to within 6% for the total fluence and 27% for the scattered fluence alone. The measured fluence was larger than the calculated value, and the reason for this discrepancy, which was primarily in the fast neutron region, was thought to be the omission from the model of scattering material, e.g. struts and supports, near the source and/or detector. This original model is discussed in more detail in Section 6.

3. THE AIM OF THE PROJECT

Because of the importance of obtaining a consistent and correct set of scatter corrections for use in the low-scatter facility during the calibration of area survey meters and the irradiation of personal dosemeters the work outlined above was extended. More detailed modelling of the irradiation facility was undertaken, more spectrum measurements were performed, and the results of a whole host of previous area survey meter calibrations evaluated.

4. EVALUATION OF AREA SURVEY METER CALIBRATIONS

The records for all area survey meter calibrations performed in the low scatter facility since 1989, together with results from investigations performed at NPL in 1982 and 1988, were studied to determine their measured scatter fractions and how they varied with distance. The results for this evaluation are shown in Figures 2 - 6, and represent data for the calibrations of four area survey instruments: the Harwell 0949, the NE Mk7 NRM and the Studsvik 2202D, calibrated with both ^{252}Cf and ^{241}Am-Be sources, and also the NE NM2 calibrated with ^{252}Cf. Because the Mk7 NRM and the 0949 are essentially the same instrument (only the electronics being different), they have been shown on the same plots and treated as a single data set for the purposes of fitting.

All of the curves show reasonable consistency and a remarkable linearity. There are, however, three significant outliers in the 0949 / Mk7 NRM plot for Am-Be (Figure 2). Although these outliers have small uncertainties, there is still the possibility that they are statistical anomalies. More realistically, it is possible that some additional source of scatter was present in the vicinity of the measurement, for example the NPL long counter, which is a physically large device, may have been too close to the source or detector.

The fits shown on the figures were performed using the scientific graphical package ORIGIN™ version 3.5[6], using a linear fit with inverse-variance weighting.

The abundance of measurements in the combined 0949 / Mk7 NRM data set for calibrations using ^{241}Am-Be made it possible to investigate the potential influence of such parameters as shadow cone used and source encapsulation on the measured scatter fraction. These are shown in Figures 7 and 8. Both these figures show that the outlier at ~165 cm is unique, inasmuch as it is the only measurement in this group to use either shadow cone #1 or source 1092. However, measurements performed using shadow cone #1 in the ^{252}Cf / Studsvik data set show no such anomaly, and it is difficult to see why a specific source should give anomalous results unless it was under-shadowed.

Similar observations can be made for the two outliers at ~90 cm. The shadow cone used (#8) is unique to these two points in this data set, however, its use in the ^{252}Cf / Studsvik data set shows no significant deviation from the other data points (although it could be argued that the values are marginally higher than other nearby values). The source used for these two outliers was, however, used for a point at ~330 cm, and agrees well with a second point at that distance. Consequently, either the results must be attributed to statistical outliers, or to a degree of under-shadowing.

Outliers aside, there is no evidence for either the choice of source or of shadow cone influencing the measured fractional scatter component.

5. BONNER SPHERE SPECTRAL MEASUREMENTS IN THE LOW-SCATTER AREA

Although the approach of using a Monte Carlo transport code to calculate the neutron scatter component, and hence derive the total neutron spectrum at any distance from a neutron source, is a very attractive one in terms of the useful and fundamental data obtained, any such calculations need to be validated against experimental measurements. With a facility which is as complex as the low-scatter area of the Chadwick Building some benchmark checks are essential to ensure that the correct materials are being used, in particular for the composition of the floor, walls, and ceiling of the room, and that the important structures within the room have been identified and included adequately in the calculational model. The best benchmark test is a comparison against measured spectra at various distances from the neutron source. Because, as indicated above, there are a number of parameters in the calculational model whose importance to the final calculated spectra are uncertain, it is important to have benchmark spectra at more than one distance from the neutron source since a particular spectrum, at a particular distance from the source, could be produced by various slightly different model configurations. Much more credence can thus be given to a calculational model which predicts correctly the spectrum at a number of distances compared to one which has only been validated against a single measured spectrum.

A Bonner sphere (BS) set was used to measure benchmark spectra at three distances, namely 150 cm, 300 cm, and 450 cm, from a ^{252}Cf neutron source positioned at the normal calibration position in the low-scatter area. This type of spectrometry system, see Awschalom and Sanna[7] and references therein for a general description, provides the only practical means of measuring a neutron spectrum over the full energy range of interest extending from thermal energies, at about 25 meV, up to several MeV. BS systems unfortunately only provide rather poor energy resolution, but this is adequate for most radiological protection applications, and also for the type of measurements undertaken here where the initial neutron source spectrum covers a broad energy range, and no detailed structure is expected in the final spectrum.

A spectral determination with a BS system involves making measurements with a thermal neutron detector positioned at the centre of a number of different diameter spheres of polyethylene. Each sphere plus thermal neutron detector combination has a different sensitivity to different parts of the neutron spectrum, and a measure of the overall spectrum can be unfolded from the measured count rates for the different spheres. The unfolding process is mathematically under-determined; however, evidence from international spectrometry intercomparison measurements[8] has shown that BS systems can provide very reasonable results provided the response functions for the individual spheres are well characterised.

The BS set used for the present measurements used a spherical ^3He proportional counter as the central thermal-neutron detector, and the response functions for the set have been obtained from a combination of measurements and calculations[9,10]. The full set of spheres were used, and these had diameters of: 3", 3.5", 4", 5", 6", 8", 10", 12", and 15". (Traditionally BSs are made with integral inch diameters, and these values are used as labels for the individual spheres.) In addition, measurements were made with the bare ^3He proportional counter, and with this counter covered by a cadmium shield. From these measurements the thermal component can be derived directly. The spectrum was unfolded using the STAY'SL computer code which has been shown in an international intercomparison of unfolding codes[11], to be one of the most appropriate for BS unfolding.

Sets of measurements were performed both with and without a shadow cone between the spheres and the neutron source. In this way both the scattered spectrum, or to be completely precise, the 'behind shadow cone spectrum', and the total, i.e. scattered plus direct, spectra were determined. In principle, the direct spectrum, i.e. total minus scatter, can also be unfolded, however, the ^{252}Cf spectrum is very well known, being a spectrum standard, and the value of the direct fluence is also known from the source emission rate. The direct data does give a useful check of the BS response functions and provided a good integral check of the measurements.

The six spectra measured, three total spectra and three scattered spectra, were used to validate and fine tune the Monte Carlo calculations. Because of the poor resolution and the under-determined nature of BS unfolding, the spectral results obtained with the system do not on their own provide an exact measure of the spectral shape which can be used with complete confidence. The approach to validating the calculations was therefore to take a calculated spectrum and use this as the starting point for unfolding the BS data, i.e. as the *a priori* guess spectrum. If the calculation provides a good measure of the spectrum the unfolding process will indicate this by having a small value for the goodness of fit, i.e. the χ^2, and will not alter the spectral shape or the normalisation. By studying any changes introduced by the unfolding, e.g. a general increase in the spectrum in the thermal region, information can be obtained on the extent to which the calculation agrees with the measurement, and also indications are obtained of the regions in which the calculations are deficient.

6. MODELLING THE IRRADIATION FACILITY USING MCNP

MCNP is a flexible Monte Carlo neutron/photon/electron transport code developed at the Los Alamos National Laboratory in New Mexico, USA and the official European outlet for the code is the NEA Data Bank in France[1].

The original MCNP model used in the earlier work described in ref(4) included the basics of the irradiation facility, but had omitted a significant amount of scattering material near the pit centre. There were no detector or shadow cone stands, and it lacked some material near the detector carriage arms (i.e. the caterpillar-track cable tray and the steel guide rod for the detector trolley).

Although not incorporated into the full model, a subsidiary model had been created, looking specifically at the material near the pit centre. This included a basic detector stand (but no supporting fins), a basic shadow cone stand (but no legs) and a basic source stand. Also included were the detector trolley support tubes and a low density (Aerolam) walkway, which had been present in the original model. This model yielded a scatter fraction of 12% at 150 cm. However, assessing the total scatter by summing the two scatter components can only be an approximation, as there are structures common to both models, rendering the answers non-additive.

Even when considering the two partial models used previously, some potentially significant structures had been omitted: there was no circular ring around the pit area, or steel support girders, or any support for the Van de Graaff beam line.

In summary, the changes resulted in a much more complicated model. The present 150 cm model used 139 cells (44 originally), 267 surfaces (79 originally) and 10 materials (6 originally). A listing of the new model for ^{252}Cf at 150 cm may be found in Appendix 1

Another alteration, with significant consequences, was the choice of concrete composition. Table 1 compares that used in the original model with several other concretes:

Table 1: Atomic composition of a number of concretes

Description	Old NPL	Portland	Maerker & Muckenthaler	Allen et al	Blizard & Abbot	Los Alamos
Source	CIRA EXT004[4] p13	ECRS[12] p178	ECRS[13] p335	ECRS[13] p337	ECRS[13] p346	MCNP4A Manual[14] p318
H	17.98	16.88	12.30	16.87	4.07	8.48
O	54.54	56.24	62.08	56.27	60.67	60.41
Si	21.73	20.41	15.45	24.72	13.90	24.19
Al	2.29	2.14	-	2.14	-	2.48
Fe	0.46	0.43	-	-	-	0.47
Ca	1.73	1.87	10.17	-	12.22	2.05
Mg	-	0.14	-	-	-	0.28
C	-	0.14	-	-	9.13	-
Na	1.27	1.18	-	-	-	0.95
K	-	0.57	-	-	-	0.69

OECD Nuclear Energy Agency Data Bank, Le Seine Saint-Germain, 12 boulevard des Îles, 92130 Issy-les-Moulineaux, France

It can be seen that the hydrogen content of the concretes varies by a factor of four, with the 'Old NPL' concrete having the highest value. In reality this is unlikely to be the case. The water content (and hence the hydrogen content) of concrete falls as the concrete ages. That forming the shielding around the Main Bay is mostly more than 30 years old. Furthermore, although the exact composition of the Main Bay concrete is unknown, it is definitely high aggregate concrete. This means that it has a higher gravel/stone chip content than usual concretes.

The effect of the different compositions on the magnitude of the scatter component were investigated using a simple model consisting of a spherical shell of the concrete, 10 metres inner diameter and 0.5 metres thick. A point ^{252}Cf source was placed at the centre of the model and the total and uncollided fluences tallied 1.5 metres away using the MCNP point detector. The results are shown in Table 2 below:

Table 2: Variation in scatter fraction with concrete composition for a spherical model of inner diameter 10 m.

Concrete	Total Fluence	Uncollided Fluence	Scatter (%)
Old NPL	$(4.240 \pm 0.037)\times10^{-6}$	3.480×10^{-6}	17.92 ± 0.16
Portland	$(4.199 \pm 0.006)\times10^{-6}$	3.480×10^{-6}	17.12 ± 0.02
Maerker & Muckenthaler	$(4.276 \pm 0.009)\times10^{-6}$	3.480×10^{-6}	18.62 ± 0.04
Blizard & Abbot	$(4.517 \pm 0.014)\times10^{-6}$	3.480×10^{-6}	22.96 ± 0.07
Los Alamos	$(4.397 \pm 0.009)\times10^{-6}$	3.480×10^{-6}	20.86 ± 0.04

It can be seen from Table 2 that, with one exception, decreasing the hydrogen content of the concrete actually increases the scatter component. This is because neutrons that undergo scatter with hydrogen always scatter in the forward direction, i.e. *into* the concrete. The fact that Portland cement goes against that trend is believed to be caused by the presence of iron offsetting the reduction in hydrogen content.

Figure 9 shows the neutron spectra for the above concrete types, with the exception of Portland, which was omitted due to its similarity to the Old NPL concrete. It can be seen that, to a greater or lesser extent, the three new concretes resulted in enhanced fast scatter peaks, reduced thermal peaks and enhanced intermediate components when compared to the original model.

It was decided to incorporate the Los Alamos concrete composition into the new model because it was the one featured in the MCNP manual and was used for MCNP neutron transport calculations, precisely the application required at NPL. There were also pragmatic reasons for its incorporation into the model, as it resulted in predicted scatter spectra closer to the measured spectra.

Another change was the inclusion of a composition for brick[15], specifically for the outer part of the one wall of the Main Bay that is an outside wall (cell 205 in the models).

One final alteration was made after a preliminary run of the 150 cm model for ^{252}Cf. The thermal peak in the output spectrum was too high, by a factor of approximately 50%. This was corrected for by the inclusion into the concrete composition of ^{10}B at the 20ppm level, equivalent to a natural boron level of 100ppm. This was considered justifiable as there could easily be borosilicates in the aggregate mixture, and possibly in the overlying plaster. The test case subsequently performed showed an improvement in the predicted / measured thermal peak comparison, with the MCNP value still being marginally higher. However, further manipulation of this boron level in order to achieve even better agreement was felt unjustifiable.

New models for irradiations based on the detector carriage system using the arm normally used for source irradiations (Arm 'C', located between the NPL and DePangher Long Counters) were created at the following distances: 115 cm, 150 cm, 200 cm, 250 cm, 300 cm, 350 cm, 400 cm and 450 cm. In each case the detector stand/trolley had to be repositioned at the appropriate distance, which involved the redefinition of 17 geometric surfaces in each case. Furthermore, four variants of the models were created at each distance, using two different sources (^{252}Cf and ^{241}Am-Be, including anisotropic source terms for X35 and X3 encapsulations respectively), with and without shadow cone.

Each model was run for between $8x10^5$ and $1x10^6$ neutron histories, and the fluence estimated by the MCNP *point detector*, resulted in typical uncertainties on the total fluence of ~0.3%. The advantage of using the point detector in this case was the automatic tallying of the *uncollided fluence* spectrum. This meant that two values for the scatter contribution were obtained at each distance - one from the shadow cone model directly and one from the subtraction of the uncollided fluence from the total fluence in the unshadowed model. Any differences between the two answers would be of great interest in evaluating the accuracy of the shadow cone technique.

7. RESULTS FROM MCNP

7.1 Comparison of predicted spectra with experimental measurements

Comparisons between the measured and the predicted, i.e. calculated, integral fluences at 150 cm, 300 cm and 450 cm for a ^{252}Cf source are shown in Table 3:

Table 3: Comparison of Integral Fluences for Measured and Predicted Spectra

Configuration	Total Spectra			Spectra behind Shadow Cone		
Distance	150 cm	300 cm	450 cm	150 cm	300 cm	450 cm
Predicted / Measurement	1.006	1.025	1.057	0.987	1.039	1.075

This shows that the agreement is, in general good: the largest discrepancy being at 450 cm behind shadow cone where predicted is 7.5% greater than measured. At 150 cm, however, the disagreement behind shadow cone is only 1.3%, with the predicted less than the measured, c.f. 27% in the original model - or 15% if additivity is assumed in allowing for the secondary model's 12% scatter contribution. The trend is clear: the scatter component is increasingly being overpredicted with increasing distance. The ratios of the predicted to the measured scatter fractions, however, agree to within 2%, being 0.981, 1.014 and 1.017 at 150 cm, 300 cm and 450 cm respectively, although there is still an apparent increase with distance.

The measured and predicted total spectra are compared in Figures 10 - 12, and those for the scatter behind shadow cone in Figures 13 - 15. All spectra are plotted as group fluences normalised to a single source neutron. Since the bins are all of equal lethargy width, the shape of the spectra would be identical in a fluence per unit lethargy or an $E.\phi(E)$ representation. Figures 10 - 12 all show the same trend: the measured spectra show a slightly broader fast neutron peak, with a slightly lower mean energy than the predicted values. This may simply reflect the low resolution of the Bonner sphere spectrometry system; furthermore it must be remembered that the response functions for the Bonner spheres themselves are not perfect.

Observations regarding the lower energy regions of the spectra are best made with respect to the scatter spectra featured in Figures 13 - 15. It can be seen that the thermal neutron region is essentially correct in all three cases; however, at intermediate energies, the predicted fluences are all slightly high. The fast neutron scatter shows some variation: in Figure 13 (150 cm) the predicted fast neutron component is roughly 10% lower than measured. This may reflect the continuing omission of some scattering material near the source, perhaps around the Van de Graaff beam line. The magnitude of the predicted fast neutron scatter at 300 cm (Figure 14) is very good, with the measurement being slightly broader, and with a slightly higher mean energy. The results shown in Figure 15 (450 cm) are broadly in agreement with those at 300 cm: the measurement favouring a slightly higher mean energy, but with marginally less neutrons.

Overall, the agreement between the predictions and the measurements is very good.

7.2 Comparison of predicted scatter fractions with previous calibrations

The predicted fluence scatter fraction results are summarised in Figure 16, which shows the variation in the calculated scatter fraction with distance for both source types, for both methods of determining the scatter component. The figure shows a distinct difference in the results from the two methods for both source types. This is not surprising, as the shadow cone will shadow some scatter from material in the room behind the source as viewed from the detector position, and will also cast a neutron shadow on one wall of the irradiation facility which, at larger distances may be significant. However, this represents a worst-case discrepancy, as the modelled detectors are vanishingly small points. In reality, any detector undergoing calibration will cast its own neutron shadow onto the wall during the 'total' irradiation. Nevertheless, this result does emphasise the care that must be taken in selecting the shadow cone used during an irradiation, so that the detector is not significantly overshadowed.

From the point of view of calibrating area survey meters, the quantity of interest is the ambient dose equivalent ($H^*(10)$) rather than the fluence. Figure 17 shows the predicted scatter fractions in terms of $H^*(10)$. Not surprisingly, the trend is the same as the fluence case, but what is surprising is that it has roughly the same magnitude, i.e. approximately a 10% discrepancy.

It is also possible to fold the known response functions of area survey meters with the spectra in order to predict the effects for specific instruments. Reasonable response function data exists for several instruments, including the NE Mk7 NRM, the Harwell 0949 (essentially identical to the Mk7 NRM) and the Studsvik 2022D. Furthermore, these results can be compared to the measured data collated for calibrations carried out since 1989, and the NPL investigations carried out in 1982 and 1988. Comparisons for the instruments 0949/Mk7 NRM and the Studsvik are shown in Figures 18 and 19 respectively, where it can be seen that there is better agreement between the measurements and the predicted <u>total</u> scatter fraction, rather than with the scatter fraction behind shadow cone.

There are several possible reasons for this discrepancy:

There is still some scattering material missing from the model. This is certainly true at 150 cm, as was demonstrated in Figure 13 where, at higher energies (the region where the area survey meters are most sensitive), the measured scatter fraction is perhaps 10% higher than the predicted, and may reflect the model's lack of scattering material around the Van de Graaff beam line assembly. However, this is not the case at 300 cm and 450 cm, where the predicted scatter at higher energies is, if anything, greater than that measured. This would suggest that other factors are responsible.

There may be some systematic error in the known instrument response functions. It is accepted that these are far from perfect. There is clearly an anomaly in the response function of the NM2, as shown in Figure 20. The discrepancy in this case indicates that the NM2 response function used in these calculations is higher than the instrument's true response function in the lower energy region.

It is, however, unlikely to be caused by source anisotropy. The measured scatter fractions were derived from raw count rate data in a similar way to the results from MCNP. The effects of the source anisotropy should therefore be present in both the experimental and the theoretical results. Furthermore, as demonstrated earlier, there is no evidence for the choice of source affecting the value of the scatter fraction.

Although MCNP calculations comparing the consequences of using source terms with and without anisotropy show slightly lower scatter fractions for those runs that included it, the effect is small (commensurate with increasing the direct component of the total measurement by the value of the anisotropy factor) and is therefore unable to explain the observed differences.

Finally, there may not be a discrepancy at all. If the shadowing during the measurement was almost perfect, the resulting scatter fraction would be much closer to the true scatter fraction than the value for the point detector behind shadow cone.

In reality, several of the above factors are probably present to a greater or lesser extent.

7.3 Calculations at 75 cm source-detector-distance relevant to personal dosemeter calibrations

The combination of MCNP calculations and experiment have recently been used to investigate the backscatter effect of 30 cm x 30 cm x 15 cm ISO and ICRP phantoms on the response of a number of personal dosemeters for both ^{241}Am-Be and ^{252}Cf sources[16]. Summarising the results, a fluence backscatter fraction of 0.8 times the direct fluence only produced of the order of a 5% increase in the response of the personal dosemeters per unit of direct fluence. In other words, although eighty neutrons were backscattered through the dosemeters for every hundred neutrons that impinged on them directly from the source, the resulting increase in the number of tracks counted was only five in one hundred, i.e. the dosemeters had an efficiency to backscattered neutrons sixteen times lower than to direct neutrons regardless of the source type, phantom type or dosemeter type put under test. This is due, in part, to the degraded energy of the neutrons but, more importantly, to their angular distribution.

As a corollary to this study, an MCNP model of the low scatter facility was adapted so that the effects on the scatter levels of the presence / absence of an ICRU (PMMA) phantom whose front face was 75 cm away from the source centre (^{252}Cf) could be investigated. The simpler of the two models, with no phantom (known as free-in-air), involved tallying the total and the uncollided fluences at 75 cm from the source. The other model, however, was slightly more complicated, involving the redefinition of the cells containing air in the vicinity of the phantom and its stand. Furthermore the contribution of the phantom itself to the total fluence at the centre of its front face had to be tallied. This is actually very straightforward in MCNP and only requires the definition of an extra tally to store the phantom's contribution to the total fluence separately. The scatter component in this case can then be deduced by subtracting the phantom and direct contributions from the total fluence.

The scatter level determined by MCNP for the free-in-air case at 75 cm was (7.6±0.1)% of the of the total fluence, or 0.082 times the direct fluence. Given that the scattered neutrons will have a very broad angular distribution, it is possible to use an efficiency for their detection by personal dosemeters similar to that observed in the phantom backscatter project, i.e. of 5/80, or 0.0625. This means that the scattered neutrons will only account for 0.5% of the total personal dosemeter response for free-in-air irradiations.

Similar calculations for the on-phantom model yielded a scatter fraction of (2.86 ±0.10)% of the total fluence, or 2.94% of the combined direct and phantom-backscattered fluence. Applying the same dosemeter efficiency as used above, this yields a scattered neutron contribution to the overall dosemeter reading of 0.2%.

Given the uncertainties on the individual readings of personal dosemeters, these scatter levels may be considered negligible.

8. CONCLUSIONS

The MCNP model of NPL's low scatter neutron irradiation facility has been validated by comparison with experimentally determined spectra and found to agree to better than 8%, even for the scatter-only measurements. This lends confidence to the predictions. Comparison of the scatter predicted behind shadow cone is lower than the true scatter as predicted in the unshadowed model by between ~5% and ~10%, for both fluence and ambient dose equivalent values. As a consequence of this it is recommended that an additional correction be incorporated into the calibration of area survey instruments, applied by multiplying the measured scatter component by 1.05 ± 0.05. This value reflects the finite size of real area survey meters and allows for a degree of 'self-shadowing' of an area on the wall during the total measurement.

This fixed factor is clearly a blanket correction and will need further investigation if a reduction in the associated uncertainty is required.

Acknowledgements

This work was funded by the UK National Measurement System Policy Unit and was Deliverable (ii) of Project 3.1 in its 1995 to 1998 Programme for Ionising Radiation Monitoring Metrology. The title of the project was: *Report on the comparison between calculated and measured results and documentation of a definitive set of scatter components in support of the calibration of personal dosemeters and area survey instruments.*

REFERENCES

1] International Organization for Standardization, *Procedures for calibrating and determining the response of neutron measuring devices used for radiation protection,* International Standard ISO 10647, 1996.

[2] International vocabulary of basic and general terms in metrology, 2nd edition. International Organisation for Standardization, 1993.

[3] EISENHAUER, C.M. Review of Scattering Corrections for Calibration of Neutron Instruments. *Radiat. Prot. Dosim.*, 1989, **28**(4), 253-262.

[4] NAISMITH, O.F. and THOMAS, D.J. MCNP Calculation of Neutron Scatter in the Main Bay of the Chadwick Building, NPL. *NPL Report CIRA(EXT)004,* February 1996.

[5] BRIESMEISTER, J.F. MCNP - A General Monte Carlo Code for Neutron and Photon Transport (Version 3a). *Los Alamos Report LA-7396-M, Rev. 2,* September 1986.

[6] Origin™ Technical Graphics and Data Analysis in Windows™. Version 3.5 MicroCal Software, Inc.

[7] AWSCHALOM, M. and SANNA, R.S., Applications of Bonner Sphere Detectors in Neutron Field Dosimetry, *Radiat. Prot. Dosim.* ***10****, 89-101, 1985.*

[8] THOMAS, D.J., CHARTIER, J-L., KLEIN, H., NAISMITH, O.F., POSNY, F., and TAYLOR, G.C., Results of a Large Scale Neutron Spectrometry and Dosimetry Comparison Exercise at the Cadarache Moderator Assembly, *Radiat. Prot. Dosim,* ***70****, 312-322, 1997.*

[9] ALEVRA, A.V., COSAK, M., HUNT, J.B., THOMAS, D.J., and SCHRAUBE, H., Experimental Determination of the Response of Four Bonner Sphere Sets to Monoenergetic Neutrons (II), *Radiat. Prot. Dosim,* ***40****, 91-102, 1992.*

[10] THOMAS, D.J., ALEVRA, A.V., HUNT, J.B., and SCHRAUBE, H., Experimental Determination of the Response of Four Bonner Sphere Sets to Thermal Neutrons, *Radiat. Prot. Dosim,* ***54****, 25-31, 1994.*

[11] ALEVRA, A.V., SIEBERT, B.R.L., AROUA, A., BUXEROLLE, M. GRECESCU, M., MATZKE, M., MOURGUES, M., PERKS, C.A., SCHRAUBE, H., THOMAS, D.J., and ZABOROWSKI, H.L., Unfolding Bonner-Sphere Data: A European Intercomparison of Computer Codes, PTB Braunschweig Report PTB-7.22-90-1, January 1990.

[12] HUBBELL, J.H. and BERGER, M.J. Photon Attenuation. *Engineering Compendium on Radiation Shielding Volume 1 Shielding Fundamentals and Methods,* edited by R.G. Jaeger, E.P. Blizard, A.B. Chilton, M. Grotenhuis, A. Hönig, Th.A. Jaeger and H.H. Eisenlohr, Berlin, Springer-Verlag, 1968, 167 - 258.

[13] SELPH, W. Neutron Attenuation. *Engineering Compendium on Radiation Shielding Volume 1 Shielding Fundamentals and Methods,* edited by R.G. Jaeger, E.P. Blizard, A.B. Chilton, M. Grotenhuis, A. Hönig, Th.A. Jaeger and H.H. Eisenlohr, Berlin, Springer-Verlag, 1968, 259 - 362.

[14] *Documentation for CCC-200/MCNP 4 Code Package.* Los Alamos National Laboratory, Los Alamos, New Mexico, October 1991.

[15] MAYNARD, M.J. Assessment of neutron Dose equivalent rates in the vicinity of Building 47. *ANS Technical Note J501-1*, June 1984.

[16] THOMAS, D.J., BARTLETT, D.T., BURKE, M., HORWOOD, N., TANNER, R. and TAYLOR G.C. Response characteristics of PADC track-etch and NTA film neutron personal dosemeters for backscatter from standard calibration phantoms. *NPL Report CIRM 7*, October 1997.

GLOSSARY

dose equivalent: is the product of Q and D at a point in tissue, where D is the absorbed dose and Q is the quality factor at that point. The special name for the unit of dose equivalent is the sievert (Sv)

effective centre: the point within the instrument at which its reading, for a particular radiation field, behaves as if it were a point detector; that is, its reading varies with the inverse square of distance from a point source in a free field situation. For a spherically symmetric instrument, this will generally be its geometric centre.

fluence response: the reading of an instrument divided by the best estimate of the fluence.

fluence to dose equivalent conversion factor (for a source): factor obtained by folding the energy-dependent fluence-to-dose equivalent conversion function over the energy spectrum of the source.

fluence (or ambient dose equivalent) calibration factor: the ratio of the value of the reference quantity (neutron fluence or ambient dose equivalent) to the instrument reading (i.e. the reciprocal of the instrument response).

free field fluence response: the fluence response which would exist if irradiations were performed in free space with no scatter or background effects.

Monte Carlo neutron transport code: a computer program that simulates the object/environment being modelled by tracking neutrons through a number of interactions, the outcome of which are determined randomly.

neutron scatter: neutrons contributing to the neutron fluence at a given location that have arrived by indirect means, i.e. following interactions with the walls/floor/ceiling, air and/or room fixtures.

neutron scatter fraction: the level of **neutron fluence scatter** expressed as a fraction of the total fluence at a given point

point detector: a form of tally in MCNP that works by calculating the probability that a neutron interaction anywhere in the system will result in a neutron travelling in the direction of the point detector, and of arriving there without undergoing further collisions.

shadow cone technique: method of determining the **neutron scatter** at a given location. The solid angle subtended by the instrument from the source is blocked by neutron scattering/absorbing materials (usually in the form of a 50 cm long cone) such that no neutrons directly from the source can impinge on the device, but allowing neutrons scattered by the air, room and/or fixtures to impinge on the instrument unhindered. The results of such a measurement can be subtracted from an equivalent measurement performed without the cone present to determine a scatter-corrected fluence at the position of the device.

uncollided fluence: a secondary tally of the MCNP **point detector** that stores the fluence at the point of interest that is directly attributable to the neutron source without any interaction whatsoever.

APPENDIX 1: LISTING OF THE 150 CM MCNP MODEL FOR ^{252}CF

```
MAIN BAY SCAT CALC - 252-Cf inc. air: NEW concrete. +Point det 150cm
c
c   Walls of room:
c
201  1  -2.3  12001 -12013 13001 -13021 14001 -14002  imp:n=1  $ base below low-scatter area
c
202  1  -2.3  12001 -12020 13001 -13021 14023 -14024  imp:n=1  $ roof above low-scatter area
c
203  1  -2.3  (12001 -12013 13001 -13002 14002 -14023)
           :(12013 -12020 13001 -13002 14004 -14023)  imp:n=1  $ x-z wall next to Control
Room
c
204  10 -1.8  (12001 -12013 13020 -13021 14002 -14023)
           :(12013 -12020 13020 -13021 14004 -14023)  imp:n=1  $ x-z wall outside Main Bay
c
205  1  -2.3  12001 -12002 13002 -13020 14002 -14023  imp:n=1  $ back wall (y-z) of l-s area
c
908  2  -0.00122  12002 -12012 13002 -13020 14005 -14023
       #(-13003 -14022) #(13019 -14021) #222 #255 25001
       #748 imp:n=1  $ air in low-scatter facility
c
980  2  -0.00122 12002 -12012 13002 -13020 14002 -14005
       33109 33110 33111 33112 33113 33114 33115 33116
       #(-13003 -14022) #( 13019 -14021) #251 #252 #253 #254  imp:n=1  $ air in low-scatter
facility
c
209  1  -2.3  12019 -12020 13002 -13020 14021 -14023  imp:n=1  $ y-z wall from roof to roof
above accelerator
c
210  1  -2.3  12019 -12020 13002 -13019 14020 -14021  imp:n=1  $ roof above accelerator
c
211  1  -2.3  12012 -12013 13002 -13020 14002 -14004  imp:n=1  $ y-z wall by base below
low-scatter area
c
212  1  -2.3  12012 -12020 13002 -13020 14004 -14005  imp:n=1  $ base below accelerator /
beam-lines
c
813  0  12013 -12020 13001 -13021 14001 -14004  imp:n=1  $ below accelerator region
c
215  1  -2.3  12012 -12020 13003 -13019 14006 -14009  imp:n=1  $ floor by beam-lines /
accelerator
c
916  2  -0.00122  12012 -12019 13002 -13020 14020 -14023
       #(-14022 -13003) #(13019 -14021) #239  imp:n=1  $ air above beamlines / roof
c
917  2  -0.00122  12012 -12017 13003 -13019 14009 -14020
       #230 #235 #(-14019 11003 -11004 11005 -11006)  imp:n=1  $ air by beam-lines
c
918  2  -0.00122  12012 -12020 13002 -13019 14005 -14006
       #227 #(-12019 -13003)  imp:n=1  $ air below beam-lines
c
220  1  -2.3  (13002 -13003 12012 -12019 14005 -14022)
```

:(13002 -13003 12019 -12020 14006 -14020) imp:n=1 $ " " between l-s and accelerator area
c
821 0 12002 -12010 13002 -13003 14002 -14022 imp:n=1 $ air btw. walls (x-z) by Control Room
c
222 1 -2.3 12002 -12011 13003 -13004 14005 -14022 imp:n=1 $ inner wall (x-z) by Control Room
c
225 1 -2.3 12002 -12012 13019 -13020 14002 -14021 imp:n=1 $ inner wall (x-z) on north of low-scatter facility
c
226 1 -2.3 12012 -12020 13019 -13020 14005 -14021 imp:n=1 $ " " by outside of beamline / source cell area
c
227 1 -2.3 12019 -12020 13015 -13019 14005 -14020 #215 imp:n=1 $ source cell wall (y-z)
c
229 1 -2.3 12010 -12012 13002 -13003 14002 -14022 imp:n=1 $ part of inner wall (x-z) by Control Room
c
230 1 -2.3 12016 -12017 13005 -13007 14009 -14020 imp:n=1 $ rhs wall (x-z), accel-level, forming part of entrance maze
c
232 1 -2.3 ((13005 12017 -12018 11001):(13011 -13013 -12020 11001)
:(11001 -11002 -13011 12018)) (14009 -14020) imp:n=1 $ wall (x-z) separating VdG and source cell areas
c
235 1 -2.3 12014 -12015 13003 -13006 14009 -14017 imp:n=1 $ y-z wall forming part of entrance maze
c
937 2 -0.00122 12017 -12020 13003 -13019 14009 -14020 #227 #232 imp:n=1 $ air around accelerator
c
239 1 -2.3 14020 -14021 12017 -12019 13003 -13013
#(-13013 12017 -11001) imp:n=1 $ front part of roof over accelerator room
c
c Pit-circle and thermal pile:
c
c
c
748 7 -1.25 12002 -12012 14008 -14009 13003 -13019 25001
#(-13004 -12011) #(-12005 13017) imp:n=1 $ steel/wood grid floor
c
549 4 -0.9 14009 -14019 11003 -11004 11005 -11006 #450 imp:n=1 $ thermal pile - wax
c
450 5 -2.25 14009 -14018 11007 -11008 11009 -11010 imp:n=1 $ thermal pile - graphite
c
251 1 -2.3 12002 -12012 13003 -13008 14002 -14005 imp:n=1 $ GCT Concrete by side of pit
c
252 1 -2.3 12006 -12012 13014 -13019 14002 -14005 25002 imp:n=1 $ GCT Concrete by side of pit
c
253 1 -2.3 12002 -12006 13016 -13019 14002 -14005 25002 imp:n=1 $ GCT Concrete by

```
side of pit
c
254  1  -2.3  12002 -12007 13008 -13016 14002 -14003
       #(13009 -13012 11014) #(12006 13014)  imp:n=1  $ GCT Concrete in lower pit
c
255  1  -2.3  12002 -12005 13017 -13019 14005 -14011
       #(-13018 -12003 -14007) #(-12004 13018 -14007)  imp:n=1  $ GCT emergency exit
c
c
860  0  #(12001 -12020 13001 -13021 14001 -14024)  imp:n=0  $ neutron cut-off
c
c    CELLS FROM MESH1C
C
c    ** CELL 90:  Air z > 492.5; -123 < x < 0..............................
90   2 -0.00122 -25001 36109 14102 12107 -12129
     #(12107 -31104 -12121) #(-41101 -12126 12128) #356 #357 #362
     #(-14113 14108 12108 -12111 13109 -13108)
     #(14102 -14108 12107 -12112 13109 -13108) imp:n=1
c
c    ** CELL 91:  Air 518.2 > z > 492.5; x < -96.3................................
91   2 -0.00122 -25001 14102 -14105 -12107 #41 #(-31104 12122)
     #23 #24 imp:n=1
c
c    ** CELL 911:  Air z > 518.2; x < -96.3................................
911  2 -0.00122 -25001 14105 -12107
     #(-33103 14105 -14106) #21 #55 #57 #58 #241 #242 imp:n=1
c
c    ** CELL 92:  Air 492.5 < z < 578;  x > 0; y < 7.6....................
92   2 -0.00122 -25001 36109 14102 -14012 -13108 12129 #69 #70 #71 #72 #73
     #362 imp:n=1
c
c    ** CELL 93:  Air 492.5 < z < 578;  x > 0; y > 7.6....................
93   2 -0.00122 -25001 36109 14102 -14012 13108 12129 #74 #75 #76 #77 #78
     imp:n=1
c
c    ** CELL 94:  Air  z > 578;  x > 0................................
94   2 -0.00122 -25001 36109 14012 12129 #68 imp:n=1
c
c    ** CELL 95: Air immediately around src stand.................
95   2 -0.00122 -25001 -36109 14102 #10 #17 #18 #84 #85 #86
     #(-36007 -14012 14102) imp:n=1
c
c    ** CELL 96: Air 452.75 < z < 492.5; x<11.4.......
96   2 -0.00122 -25001 -14102 14121 -12113 #11 #12 #19 #15 #151 #152 #153
     #45 imp:n=1
c
c    ** CELL 97: Air 452.75 < z < 492.5 x > 11.4......
97   2 -0.00122 -25001 -14102 14121 12113 #131 #132 #153
     #(12137 36119 -11121 14150 -14148) $ #13 #43
     #(11012 11013 36113 14115 -14114)  $ #14 #44
     #(-14147 11109 11108 36114 -36113) imp:n=1
c    ** CELL 99: Air 437.25 < z < 452.75...................
99   2 -0.00122 -25001 -14121 14122 #26 #27 #28 #29 #39 #40 #42
     #(11109 11108 36114 -36113) imp:n=1
```

```
c
c     ** CELL 98: Air z < 437.25......................
98    2 -0.00122 -25001 14005 -14122 33109 33110 33111 33112 33113 33114
      33115 33116 #46 #47 imp:n=1
c
6     3 -7.93  -36006 36105 -14118 14112 imp:n=1  $ GCT Collar of steel block
7     0        -36105 -14118 14112 imp:n=1     $ GCT void in collar
8     3 -7.93  -36006 -14012 14118  imp:n=1    $ GCT Steel block top of lower rod
9     0  -36006 -14112 14102     imp:n=1       $ GCT void inside lower source rod
10    3 -7.93 36007 -36104 -14119 14120 imp:n=1 $ GCT Collars on source support
11    6 -2.7  -25001 32102 -32101 31101 imp:n=1      $ detector carriage tube (x2)
12    6 -2.7  -25001 -12114 31102 -31101  imp:n=1  $ detector carriage tube
14    6 -0.083  -25001 11012 11013 36113 14115 -14127 imp:n=1  $ walkway (beam-lines)
13    6 -0.083  -25001 12137 36119 -11121 14150 -14149 imp:n=1  $ walkway
131   6 -2.7  -36119  36120 12137 -11121 14151 -14149 imp:n=1  $ walkway end piece
132   6 -2.7  -36120  36121 -11125 11124 14152 46101 12129 imp:n=1   $ walkway end piece
strengthener
15    6 -0.083  -25001 -12136 36119 11120 14150 -14149 imp:n=1  $ walkway
151   6 -2.7  -36119  36120 -12136 11120 14151 -14149 imp:n=1  $ walkway end piece
152   6 -2.7  -36120  36121 -11125 11124 14152 46101 -12129 imp:n=1   $ walkway end piece
strengthener
153   6 -2.7  -36120 -11123 11122 14151 -14152 imp:n=1   $ walkway centre locater
16    3 -7.93  36006 -36007 14102 -14012  imp:n=1  $ lower source rod
17    3 -7.93  -36004 14012 -14013  imp:n=1     $ upper source rod
18    3 -7.93  -36109 36110 14102 -14103 imp:n=1 $ GCT thickening at base of src sup
19    6 -2.7   -31101 -32101 imp:n=1  $ GCT solid core of carriage tubes
c
21    3 -7.93 14106 -14107 -33101  33102 imp:n=1  $ detector support
22    3 -7.93  33102 -33103 14105 -14106  imp:n=1  $ detector stand rod
23     3 -7.93   14146 -14105 12104 -12103 13104 -13103   imp:n=1   $ steel base of detector
support
24    6 -2.7   14104 -14146 13105 -13103 12106 -12105  imp:n=1  $ Al detector carriage
241   3 -7.93 -43102 14105 33103 13119 -13120 imp:n=1          $ det. stand fins
242   3 -7.93 -43102 14105 33103 -12134 12135 -13119 imp:n=1  $ det. stand fins
25    0  -33102 14105 -14106  imp:n=1  $ inside source rod
c
26   3 -7.93 -14121 14122 -36106 36107 #(-14123 14124 -36106 36108) imp:n=1 $ GCT Pit centre
support ring
c
c     The pit centre cross girders have a reduced density to allow for their 'I'
c     shape. Actual dimensions: 12.7cm wide by 15.5cm high. Insets 6cm x 14.1cm
c     taken as 12.7cm x 15.5cm. Density should therefore be reduced to 14.05%
c     of true value. However, take height of girder to be 12.25cm. Thus take
c     working density to be 17.78% of true value.
c
27    3 -1.41 -14125 14122 -11104 11105 -36107 11106 imp:n=1 $ GCT Pit centre cross girder
28    3 -1.41 -14125 14122 -11104 11105 -36107 -11107 imp:n=1 $ GCT Pit centre cross girder
29    3 -1.41 -14125 14122 -11106 11107 -36107 imp:n=1 $ GCT Pit centre cross girder
c
c     DESCRIPTION OF SHADOW CONE STAND, etc.
c
300   2 -0.00122 -14113 14109 12108 -12111 13109 -13108 31107 $ air around s.c. stand
      #(14110 -14145 12109 -12110 13107 -13106)            $ (#331 #34)
      #(-14139 -13129) #(-14139 13130)                     $ (#351 #352)
```

```
     #(14139 -14140 -13131)  #(14139 -14140 13132)          $ (#353 #354)
     #(-33104 14145) #332 #333 imp:n=1                     $ (#30 #31 #32 #33)
301   2 -0.00122 14102 -14108 12107 -12112 13109 -13108
     #36 #361 #37 #38 imp:n=1                             $ air around s.c. legs
30    3 -7.93  14112 -14113 33106 -33104  imp:n=1            $ top of s.c. rod
31    0  14112 -14113 -33106  imp:n=1                      $ void in top of s.c. rod
32    3 -7.93  33105 -33104 14145 -14112  imp:n=1            $ s.c. rod
33    0  -33105 14145 -14112  imp:n=1                      $ void in s.c. rod
331   3 -7.93 14111 -14145 12109 -12110 13107 -13106 imp:n=1  $ s.c. Fe support base
332   3 -7.93 -43101 14145 33104 11116 -11117 imp:n=1         $ s.c. stand fins
333   3 -7.93 -43101 14145 33104 -11118 11119 imp:n=1         $ s.c. stand fins
34    6 -2.7 -14111 14110 12109 -12110 13107 -13106  imp:n=1  $ s.c. Al support base
35    3 -7.93 14108 -14109 12108 -12111 13109 -13108 imp:n=1  $ s.c. steel base (moves cone)
351   3 -7.93 14109 -14139 12108 -12111 13109 -13129 imp:n=1  $ s.c. trolley part
352   3 -7.93 14109 -14139 12108 -12111 13130 -13108 imp:n=1  $ s.c. trolley part
353   6 -2.7  14139 -14140 12108 -12111 13109 -13131 imp:n=1  $ s.c. trolley part
354   6 -2.7  14139 -14140 12108 -12111 13132 -13108 imp:n=1  $ s.c. trolley part
355   3 -7.93  -31107 12108 -12111 imp:n=1                  $ s.c. trolley thread
356   6 -2.7  13109 -13108 14141 -14142 12130 -12108 imp:n=1  $ s.c. trolley end block
357   6 -2.7  13109 -13108 14141 -14142 12111 -12131 imp:n=1  $ s.c. trolley end block
36    6 -2.7  14103 -14108 12107 -12112 13109 -13108 imp:n=1  $ Al s.c. carriage
361   6 -2.7  14143 -14103 12132 -12112 13109 -13108 imp:n=1  $ s.c. spacer block
362   6 -2.7  12112 -12133 11114 -11115 -14144 14143 13109    $ plate attaching s.c.
     -13108 36109 imp:n=1                                 $ stand to src stand
37    6 -2.7  -14103 14102 -13112 13111 -12115 12116 imp:n=1  $ Al s.c. carriage leg 1
38    6 -2.7  -14103 14102 -13112 13111 -12118 12117 imp:n=1  $ Al s.c. carriage leg 2
c
39    6 -0.083  -14128 14125 -36107 #(11109 11108 36114 -36113) imp:n=1 $ GCT aerolam over
pit centre
40    3 -7.93  -36111 36112 -14121 14126 imp:n=1    $ GCT subsidiary steel ring
41    4 -0.5   -31103 12119 -12120 imp:n=1       $ GCT revised cable 'caterpillar'
42    4 -1.0  -14121 14128 -36107 #(11109 11108 36114 -36113) imp:n=1 $ GCT hydrogenous
layer
c
43    4 -1.0  -25001 12137 36119 -11121 14149 -14148 imp:n=1        $ GCT hydrogenous
walkway cover
44    4 -1.0 -25001 11012 11013 36113 14127 -14114  imp:n=1    $ GCT hydrogenous walkway
(beam-lines)
45    4 -1.0 -25001 -12136 36119 11120 14149 -14148  imp:n=1  $ GCT hydrogenous walkway
cover
c
46    3 -7.93 -14122 14129 -36106 36113 -11104 11105 imp:n=1 $ GCT cross girder support
47    3 -7.93 -14122 14129 -36106 36113 -11106 11107 imp:n=1 $ GCT cross girder support
48    3 -7.93 11109 11108 -14147 14122 36114  -36113 imp:n=1 $ GCT Steel arc
c
55    3 -7.93  33117 -33107 -14130 14107 imp:n=1  $ GCT Detector support plate
56    6 -2.7  -12121 12122 -31104 imp:n=1  $ Det carriage locater
c
57    3 -7.93 14105 -14131 -33108 imp:n=1 $ GCT detector cable support
58    4 -0.5 -32103 32104 -13114 13113 imp:n=1 $ GCT detector cables
c
60    3 -7.93 -33109 14002 -14122 imp:n=1 $ GCT support pillar
61    3 -7.93 -33110 14002 -14122 imp:n=1 $ GCT support pillar
62    3 -7.93 -33111 14002 -14122 imp:n=1 $ GCT support pillar
```

```
63   3 -7.93 -33112 14002 -14122 imp:n=1 $ GCT support pillar
64   3 -7.93 -33113 14002 -14122 imp:n=1 $ GCT support pillar
65   3 -7.93 -33114 14002 -14122 imp:n=1 $ GCT support pillar
66   3 -7.93 -33115 14002 -14122 imp:n=1 $ GCT support pillar
67   3 -7.93 -33116 14002 -14122 imp:n=1 $ GCT support pillar
c
68   3 -7.93 31105 -31106 -25001 12123 imp:n=1 $ GCT beam tube
69   3 -7.93 11110 -11111 13115 -13116 12123 -12124 imp:n=1 $ GCT part of girder
70   3 -7.93 11112 -11113 13117 -13118 14133 -12124 imp:n=1 $ GCT part of girder
71   3 -7.93 12123 -12125 13115 -13116 11111  14133 imp:n=1 $ GCT part of girder
72   3 -7.93 12125 -11112 13117 -13118 -14132 14133 imp:n=1 $ GCT part of girder
73   3 -7.93 11111 -11112 13119 -13120  12125 14132 -12124 imp:n=1 $ GCT part of girder
74   3 -7.93 11110 -11111 13121 -13122 12123 -12124 imp:n=1 $ GCT part of girder
75   3 -7.93 11112 -11113 13123 -13124 14133 -12124 imp:n=1 $ GCT part of girder
76   3 -7.93 12123 -12125 13121 -13122 11111  14133 imp:n=1 $ GCT part of girder
77   3 -7.93 12125 -11112 13123 -13124 -14132 14133 imp:n=1 $ GCT part of girder
78   3 -7.93 11111 -11112 13125 -13126  12125 14132 -12124 imp:n=1 $ GCT part of girder
c
82   2  -0.00122  12127 -12126 -41101 imp:n=1     $  Fe
83   2  -0.00122  12128 -12127 -41101 imp:n=1     $  Borated Wax
c
84   3  -7.93  14014 -14016 -36005 36001 #(-36003 14015) imp:n=1 $ SRC Cup
85   3  -7.93  36001 -36002 14013 -14014  imp:n=1 $ SRC Cup Stem
86   0  -36003 14015 -14025 imp:n=1  $ source (x35 capsule represented by VOID)
c

c    Surfaces
11001  p   1.85   -1     0   3028
11002  p   1.79   -1     0   3183
11003  p   0.575   1     0   674.3
11004  p   0.575   1     0   882.1
11005  p   1.733  -1     0   1149
11006  p   1.733  -1     0   1780
11007  p   0.575   1     0   695.1
11008  p   0.575   1     0   861.3
11009  p   1.733  -1     0   1185
11010  p   1.733  -1     0   1744
11012  p   0.36   -1     0  0
11013  p   0.36    1     0  0
11014  p   0.228   0     1  -32.85 $ Was 0.228 0 1 -18.25
11104 p  1        1    0    8.98
11105 p  1        1    0   -8.98
11106 p -1        1    0    8.98
11107 p -1        1    0   -8.98
11108 p  1        2    0    0
11109 p  1       -2    0    0
11110 p  0.631    0   -1  -438.0
11111 p  0.631    0   -1  -437.3
11112 p  0.437    0   -1  -445.4
11113 p  0.437    0   -1  -444.7
11114 p -0.975   -1    0   -11.0125
11115 p  0.975   -1    0    11.0125
11116 p -0.6053  -1    0    22.2899
11117 p -0.6053  -1    0    23.1081
```

```
11118 p  0.6053  -1    0   -22.2899
11119 p  0.6053  -1    0   -23.1081
11120 p  2.077   -1    0    44.69   $ new in DET32F
11121 p  2.077   -1    0   -44.69   $ new in DET32F
11122 p  4.382   -1    0   -22.83   $ new in DET32F
11123 p  4.382   -1    0    22.83   $ new in DET32F
11124 p  4.382   -1    0    -5.71   $ new in DET32F
11125 p  4.382   -1    0     5.71   $ new in DET32F
c
c
12001  px  -874  $ Changed from -810
12002  px  -784  $ Changed from -720
12003  px  -692.5 $ Was -628.5
12122 px  -512.5
12004  px  -439.5 $ Was -375.5
12119 px  -420
12005  px  -379.5 $ Was -315.5
12006  px  -265.5 $ Was -201.5
12106 px  -193    $ was 180 in DET32E
12104 px  -166    $ verified in DET32F
12135 px  -150.3  $ new in DET32F
12134 px  -149.7  $ new in DET32F
12007  px  -144   $ Was -80
12103 px  -134    $ verified in DET32F
12105 px  -133    $ was 120 in DET32E
12120 px  -100
12107 px   -96.3  $ was -105 in DET32D
12130 px   -81.0  $ new in DET32E
12108 px   -77.9  $ was -90 in DET32D
12116 px   -75.8  $ was -66.3 in DET32D
12115 px   -72.0  $ was -62.5 in DET32D
12128 px   -59
12117 px   -55.8  $ was -32.5 in DET32D
12118 px   -52.0  $ was -28.7 in DET32D
12109 px   -45.2  $ was -45.0 in DET32D
12110 px   -29.9  $ was -30.0 in DET32D
12127 px   -29
12136 px   -19.4  $ new in DET32F
12111 px   -17    $ was -23 in DET32D
12102 px   -16
12132 px   -15    $ new in DET32E
12131 px   -13.9  $ new in DET32E
12121 px   -12.5
12114 px   -11.5  $ was -11.4 in DET32E
12126 px    -9
12112 px    -8    $ was -17 in DET32D
12129 px     0
12101 px     7
12133 px     7.5
12113 px    11.5  $ was  11.4 in DET32E
12137 px    19.4  $ new in DET32F
12123 px   102
12125 px   102.6
12124 px   203.5
```

```
12010  px   410
12011  px   530
12012  px   631 $ Was 620
12013  px   676 $ Was 665
12014  px   960
12015  px   990
12016  px   1100
12017  px   1510
12018  px   1630
12019  px   1830
12020  px   1890
c
c
13001  py  -1060
13002  py  -1030
13003  py  -936  $ Was -920
13004  py  -876  $ Was -860
13005  py  -810
13006  py  -770
13007  py  -720
13008  py  -548   $ Was -532
13009  py  -268  $ Was -252
13113 py   -21.25
13114 py   -18.75
13105 py   -16    $ was -16.5 in DET32E
13104 py   -14.8  $ was 15.5 in DET32E
13110 py   -11.5  $ was -11.4 in DET32E
13102 py    -8
13109 py    -7.6  $ was -7.5 in DET32D
13117 py    -6.3
13131 py    -5.1  $ new in DET32E
13107 py    -4.6  $ was -4.5 in DET32D
13111 py    -4
13115 py    -3.75
13129 py    -3.6  $ new in DET32E
13119 py    -0.3
13011  py   0
13120 py     0.3
13130 py     3.6  $ new in DET32E
13116 py     3.75
13112 py     4
13106 py     4.6  $ was 4.5 in DET32D
13132 py     5.1  $ new in DET32E
13103 py     5.5  $ was 5.0 in DET32E
13118 py     6.3
13108 py     7.6  $ was 7.5 in DET32D
13101 py     8
13123 py    13.7
13121 py    16.25
13125 py    19.7
13126 py    20.3
13122 py    23.75
13124 py    26.3
13012  py   119   $ Was -135
```

```
13013  py   120
13014  py   390    $ Was 388
13015  py   460
13016  py   619    $ Was 617
13017  py   677    $ Was 675
13018  py   737    $ Was 735
13019  py   832 $ Was 830
13020  py   863 $ Was 895
13021  py   927 $ Was 925
c
14001  pz  -50 $ was 0
14002  pz   0   $ was 50
14003  pz   73
14004  pz   210
14005  pz   260 $ Was 270
14129 pz   430.45 $ was 427.7 in DET32E
14122 pz   437.25 $ was 434.5 in DET32E
14124 pz   437.95 $ was 435.2 in DET32E
14126 pz   448.25 $ was 445.5 in DET32E
14125 pz   449.5  $ was 446.75 in DET32E ??
14123 pz   452.05 $ was 449.3 in DET32E
14128 pz   452.5  $ was 449.75 in DET32E ?
14121 pz   452.75 $ was 450 in DET32E
14151 pz   456.25 $ new in DET32F
14152 pz   458.79 $ new in DET32F
14006  pz   467
14007  pz   485
14115 pz   487    $ was 485 in DET32E
14150 pz   488.8  $ new in DET32F
14008  pz   489 $ Was 487
14147 pz   489.3  $ new in DET32F
14127 pz   489.75 $ was 489.8 in dets22
14114 pz   490
14149 pz   491.25 $ new in DET32F
14148 pz   491.5  $ new in DET32F
14009  pz   492 $ Was 490
14101 pz   492.5
14102 pz   494.51 $ was 492.05 in DET32E
14010  pz   495  $ was 490.5
14133 pz   495.6
14132 pz   496.2
14104 pz   511.5  $ was 507.5 in DET32E
14143 pz   513.5  $ was 511.1 in DET32E
14011  pz   515
14144 pz   516.0  $ was 513.6 in DET32E
14146 pz   517.5  $ new in DET32E
14103 pz   517.9
14105 pz   518.2  $ was 520.2 in DET32E
14108 pz   520.4  $ was 518.0 in DET32E
14141 pz   521.0  $ was 518.6 in DET32E
14109 pz   521.9  $ was 519.5 in DET32E
14139 pz   522.7  $ was 520.3 in DET32E
14110 pz   523.9  $ was 521.5 in DET32E
14140 pz   524.3  $ was 521.9 in DET32E
```

```
14142 pz   524.8  $ was 522.4 in DET32E
14111 pz   526.0  $ was 523.6 in DET32E
14145 pz   527.3  $ was 524.9 in DET32E
14131 pz   555.7
14106 pz   566.7  $ was 558.7 in DET32E
14107 pz   567.3  $ was 559.3 in DET32E
14130 pz   567.9  $ was 559.9 in DET32E
14112 pz   575.5  $ was 573.5 in DET32D
14120 pz   576.6  $ was 570.6
14119 pz   579.8  $ was 573.8
14113 pz   582    $ was 580 in DET32D
14118 pz   583    $ was 577
14012  pz   584
14013  pz   594.3
14134 pz   595
14014  pz   597.2
14015  pz   597.25
14016  pz   597.6
14025  pz   598.75
14017  pz   690
14018  pz   706
14019  pz   724
14020  pz   790
14021  pz   880
14022  pz   1310
14023  pz   1859
14024  pz   1874
c
22101 s -200  -20  570.7  21       $ air bubble for det cables
c
25001  sz   490  610
25002  sz   598  615               $ Was 613 (May need adjusting for z!)
c
31101 c/x     0    483.0  11.5    $ was 480.6 in DET32E
31102 c/x     0    483.0  10.2    $ was 480.6 in DET32E
31103 c/x    20    504.25  4.0    $ was 502 in DET32E
31104 c/x   -10.5  505.5   2      $ was 498.2 in DET32E
31105 c/x     0    598     1.86
31106 c/x     0    598     1.91   $ beam tube
31107 c/x     0    523.0   0.7    $ was 520.6 in DET32E
c
32101 c/y    0     483.0  11.5    $ was 480.6 in DET32E
32102 c/y    0     483.0  10.2    $ was 480.6 in DET32E
32103 c/y  -200     570.7  20     $
32104 c/y  -200     570.7  18.5   $  Cables for detector
c
33101 c/z  -150     0    10.      $ was 7.5 in DET32E
33102 c/z  -150     0     2.40    $ was 2.2 in DET32E
33103 c/z  -150     0     2.55    $ was 2.5 in DET32E
33104 c/z   -37.5   0     2.55    $ was 2.5 in DET32D
33105 c/z   -37.5   0     2.25    $ was 2.2 in DET32D
33106 c/z   -37.5   0     1.13    $
33107 c/z  -150     0    15.25    $ Steel plate
33117 c/z  -150     0     6.95
```

```
33108 c/z -161    -12    0.5   $ Detector cable support
33109 c/z  90.4    37.4  2.2   $ Support pillar
33110 c/z  90.4   -37.4  2.2   $ Support pillar
33111 c/z -90.4    37.4  2.2   $ Support pillar
33112 c/z -90.4   -37.4  2.2   $ Support pillar
33113 c/z  37.4    90.4  2.2   $ Support pillar
33114 c/z  37.4   -90.4  2.2   $ Support pillar
33115 c/z -37.4    90.4  2.2   $ Support pillar
33116 c/z -37.4   -90.4  2.2   $ Support pillar
c
36001  cz  0.2
36002  cz  0.3
36003  cz  0.475
36004  cz  0.5   $ (was 0.4)
36005  cz  0.525
36105 cz  1.9
36006  cz  2.25
36007  cz  2.5
36110 cz  3.6
36104 cz  3.75
36109 cz  5.1
36121 cz  81.5    $ new in DET32F
36114 cz  87.5    $ changed from 88.5 in GTDETS24
36113 cz  89.5
36107 cz  92.8
36108 cz  93.5
36106 cz 100
36112 cz 104.8
36111 cz 108
36120 cz 117.5    $ new in DET32F
36119 cz 120      $ new in DET32F
c
41101 k/x   9.2  0  598   7.75E-03  -1  $ Cone #1: X-value should be 18.2 more
c
43101 k/z  -37.5  0  566.8  4.15e-02  -1  $ cone for defining s.c. stand fins: was 564.4 in
DET32E
43102 k/z -150.  0  551.2  0.1024   -1  $ cone for defining det. stand fins.
c
46101 kz   428.04 4  1               $ new in DET32F

sc1  Cf-252 SOURCE (MAXWELL FISSION SPECTRUM) (x35 capsule- but void)
sdef  erg=d1 pos= 0 0 598 cel=86 rad=d2 ext=d3 axs=0 0 1 vec=0 0 1 dir=d4
sp1   -2 1.42
si2   0 0.476
si3   0.751
si4   a -1.0 -0.9848 -0.9397 -0.8660 -0.7660 -0.6428 -0.5 -0.3420 -0.1736 0
      0.1736 0.3420 0.5 0.6428 0.7660 0.8660 0.9397 0.9848 1.0
sp4   1.0445 1.0277 0.9993 0.9959 0.9947 1.0002 1.0104 1.0221 1.0170 1.0207
      1.0176 1.0085 0.9828 0.9619 0.9577 0.9536 0.9899 1.0252 1.0368
c
c
e0    7.943E-10 1.259E-09 1.995E-09 3.162E-09 5.012E-09 7.943E-09
      1.259E-08 1.995E-08 3.162E-08 5.012E-08 7.943E-08 1.259E-07
      1.995E-07 3.162E-07 5.012E-07 7.943E-07 1.259E-06 1.995E-06
```

```
     3.162E-06 5.012E-06 7.943E-06 1.259E-05 1.995E-05 3.162E-05
     5.012E-05 7.943E-05 1.259E-04 1.995E-04 3.162E-04 5.012E-04
     7.943E-04 1.259E-03 1.995E-03 3.162E-03 5.012E-03 7.943E-03
     1.259E-02 1.995E-02 3.162E-02 5.012E-02 7.943E-02 1.259E-01
     1.995E-01 3.162E-01 5.012E-01 7.943E-01 1.259E+00 1.995E+00
     3.162E+00 5.012E+00 7.943E+00 1.259E+01 1.995E+01 3.162E+01
c
fc5  POINT DETECTOR AT 150cm FROM SOURCE, ABOVE STAND
f5:n  -150 0 598 1.0
c
c    $ CONCRETE (Los Alomos- from MCNP4A manual, p318) + 20ppm 10B
m1    1001  0.0848  8016 0.6041 14000 0.2419 13027 0.0248 26000 0.0047
     20000 0.0205 12000 0.0028 11023 0.0095 19000 0.0069 5010 0.00002
c
m2    7014 0.7844 8016 0.2107 18000 0.0047 6012 0.0002  $ AIR
c
m3    26000 0.6935 24000 0.1856 28000 0.0934 25055 0.0143
     14000 0.0121 6012 0.0011  $ STEEL
c
m4    1001 0.6667 6012 0.3333 $ polythene (for cables) and wax
c
m5    6012 1.0    $ Graphite
c
m6    13027 1  $ ALUMINIUM
c
m7    26000 0.6935 24000 0.1856 28000 0.0934 25055 0.0143 $ STEEL +
     14000 0.0121 6012  0.1301  1001 0.2150 8016  0.1070 $ CELLULOSE (C6 H10 O5)
c
m8    26000 1.0   $ Fe
c
m9    1001 0.6 6012 0.3 5000 0.1  $ Paraffin Wax + 10% Boron
c
m10   13027 0.0036 20000 0.0073  26000 0.0024 8016 0.6633 14000 0.3234 $Brick
c
phys:n  31.62 31.62  $ MAX ENERGY - ANALOG CAPTURE
c
nps   1000000
```

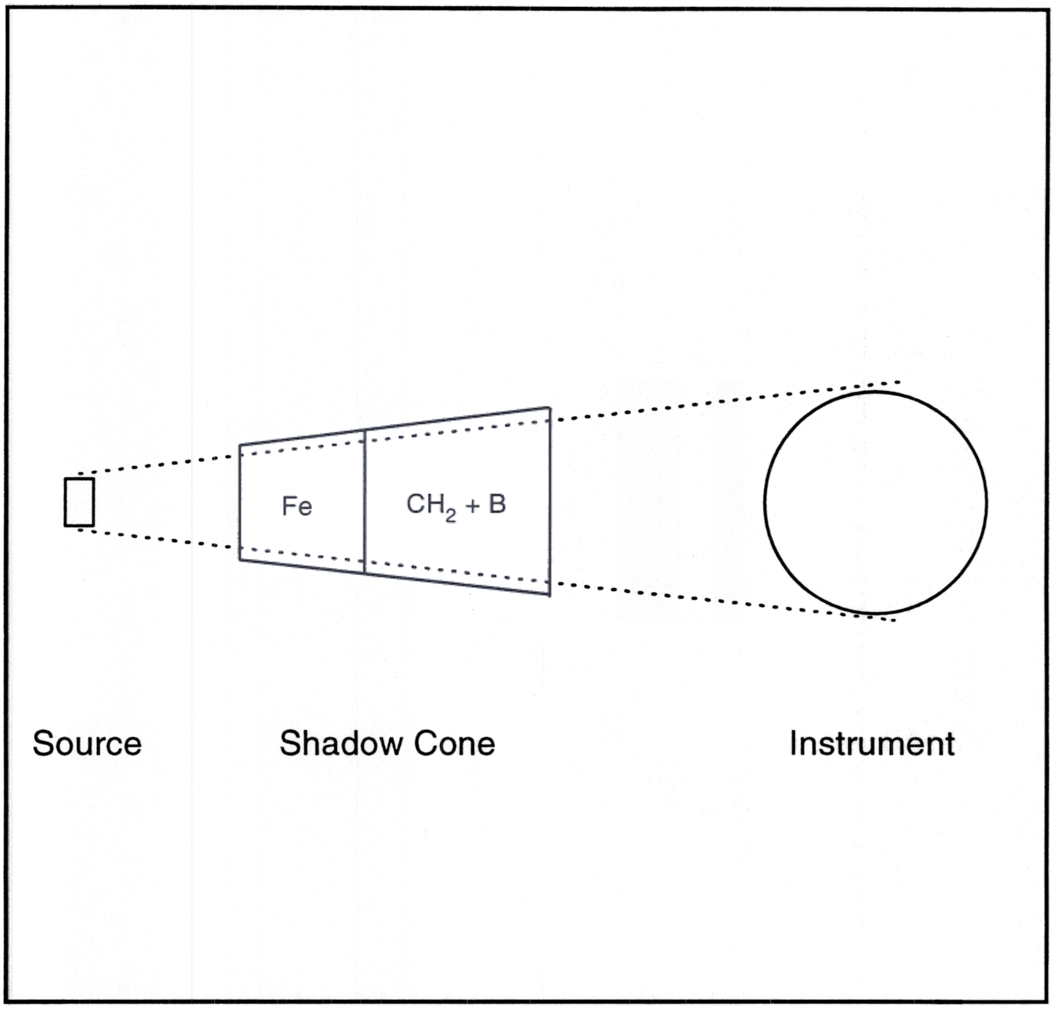

Figure 1. Schematic representation of the shadow cone method for determining neutron scatter

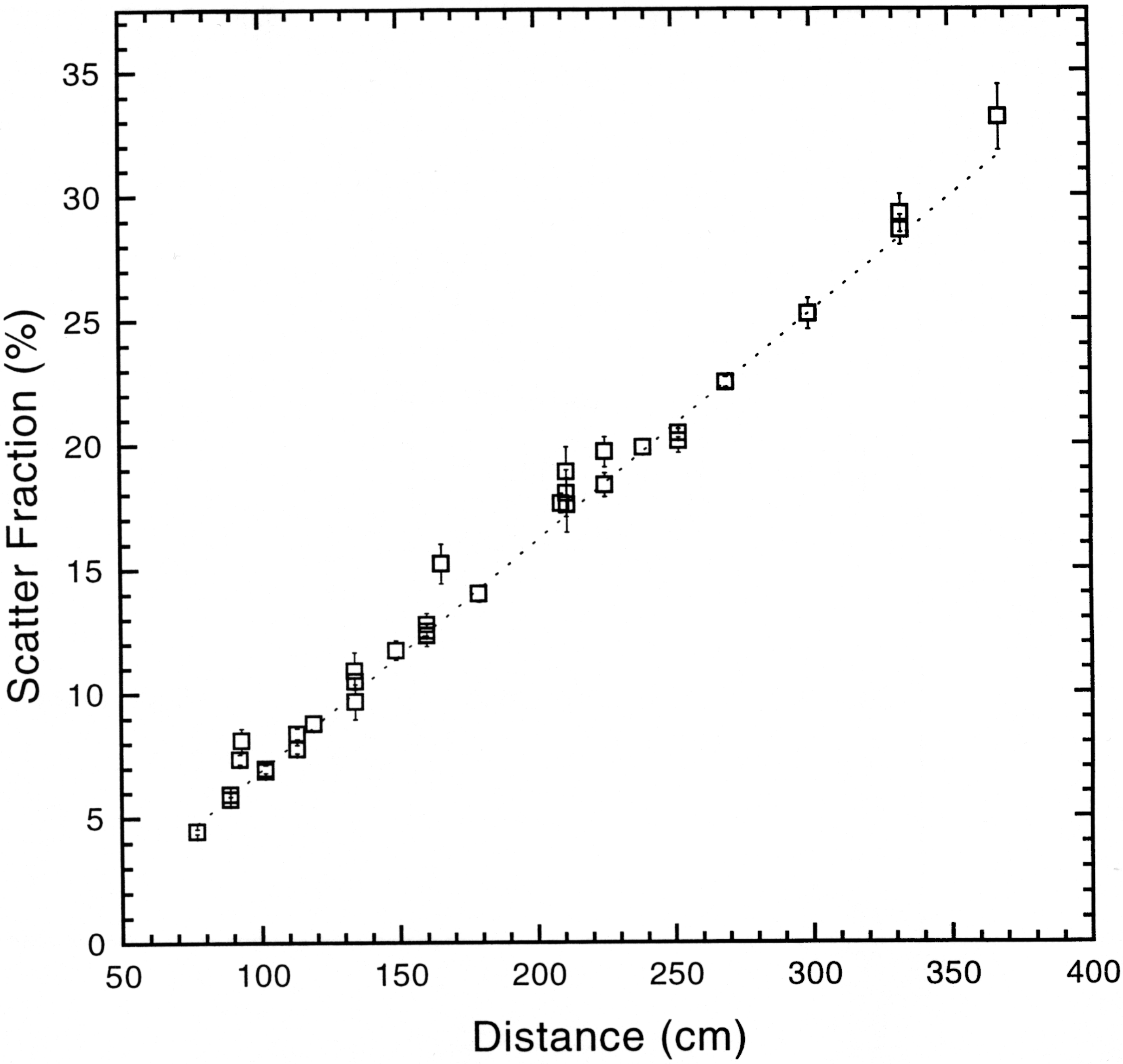

Figure 2. Variation of scatter fraction with distance measured for the 0949 and Mk7 NRM instruments for an Am-Be source.

The inverse-variance-weighted linear fit parameters are:
SF = -(2.332 +/- 0.083) + (0.09224 +/- 0.00063).D

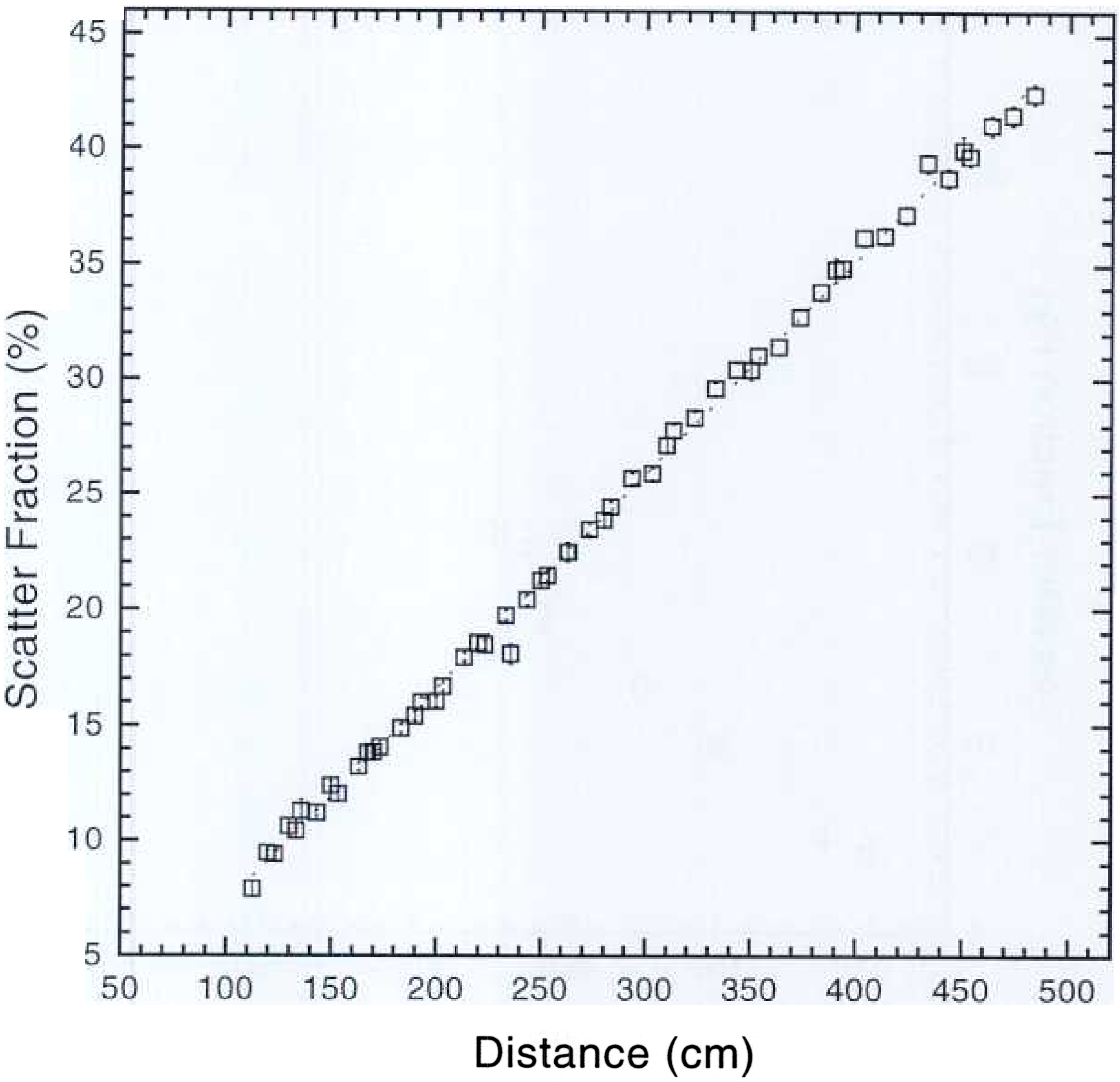

Figure 3. Variation of scatter fraction with distance measured for the 0949 and Mk7 NRM instruments for a ^{252}Cf source.

The inverse-variance-weighted linear fit parameters are:
SF = -(2.049 +/- 0.074) + (0.09318 +/- 0.00033).D

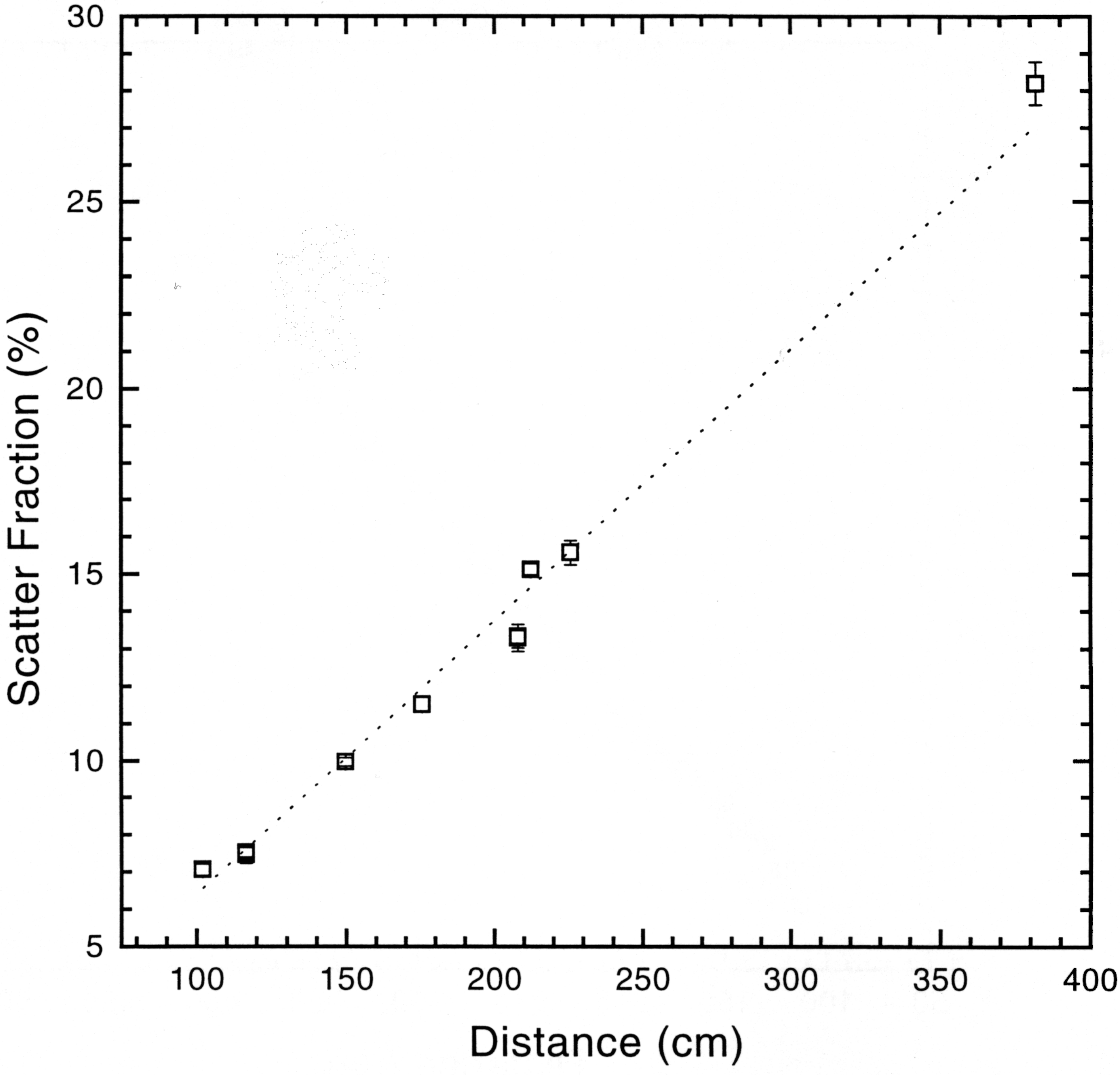

Figure 4. Variation of scatter fraction with distance measured for the Studsvik 2022D instrument for an Am-Be source.

The inverse-variance-weighted fit parameters are:
SF = -(0.90 +/- 0.20) + (0.0732 +/- 0.0013).D

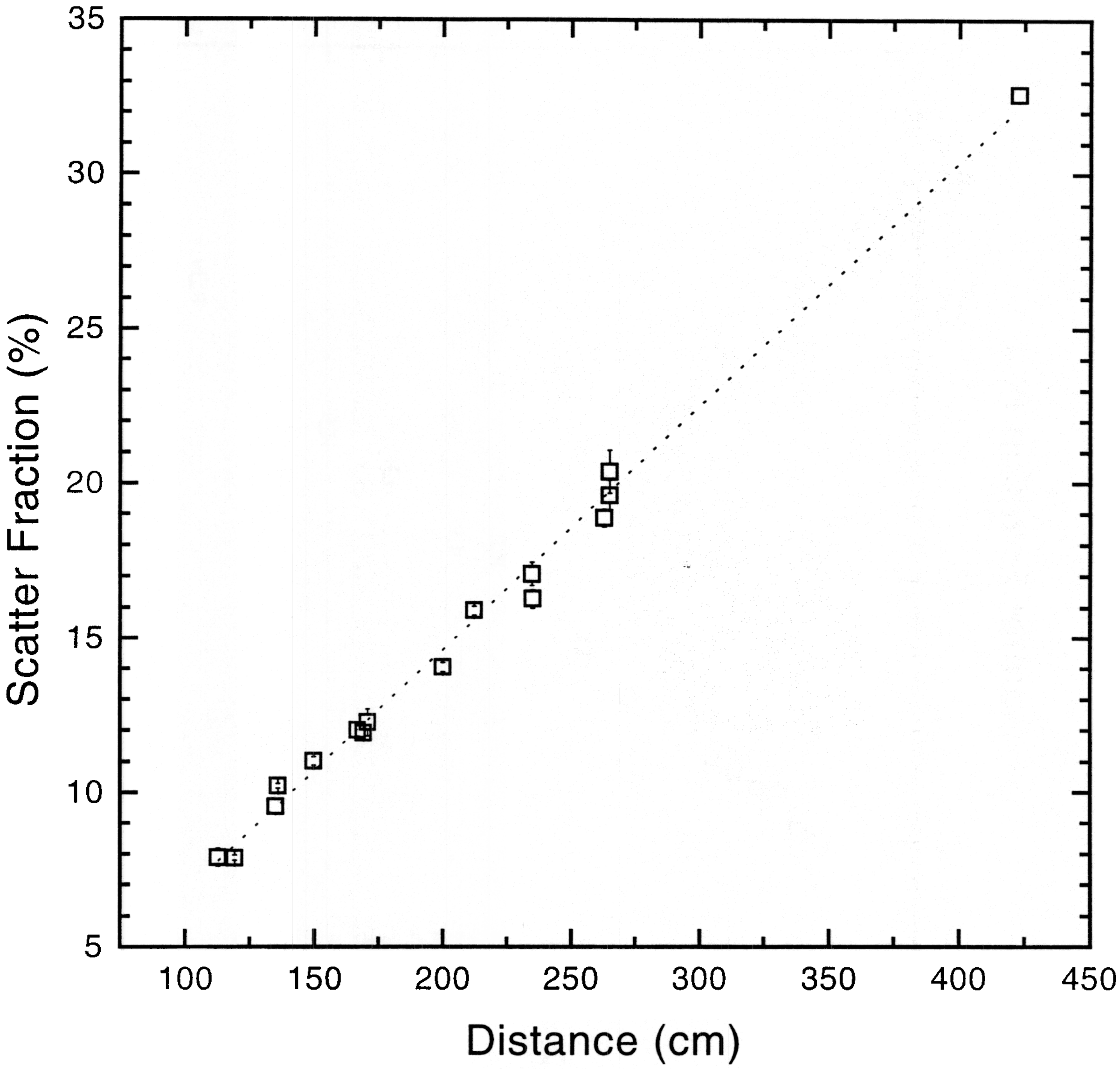

Figure 5. Variation of scatter fraction with distance measured for the Studsvik 2022D instrument for a ^{252}Cf source.

The inverse-variance-weighted linear fit parameters are:
SF = -(1.10 +/- 0.11) + (0.07867 +/- 0.00066).D

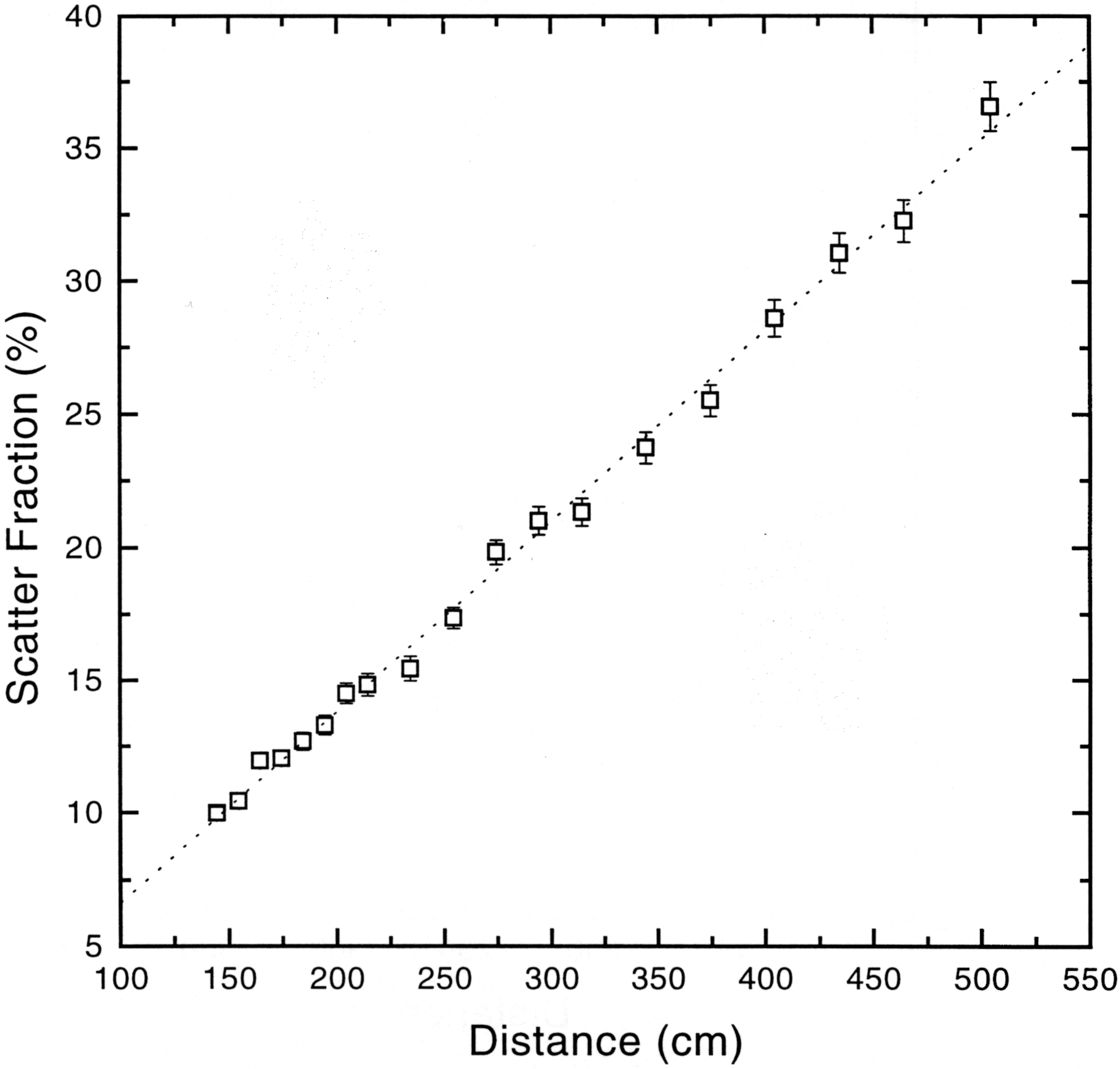

Figure 6. Variation of scatter fraction with distance measured for the NE NM2 instrument for a ^{252}Cf source.

The inverse-variance-weighted fit parameters are:

SF = -(0.55 +/- 0.34) + (0.0718 +/- 0.0011).D

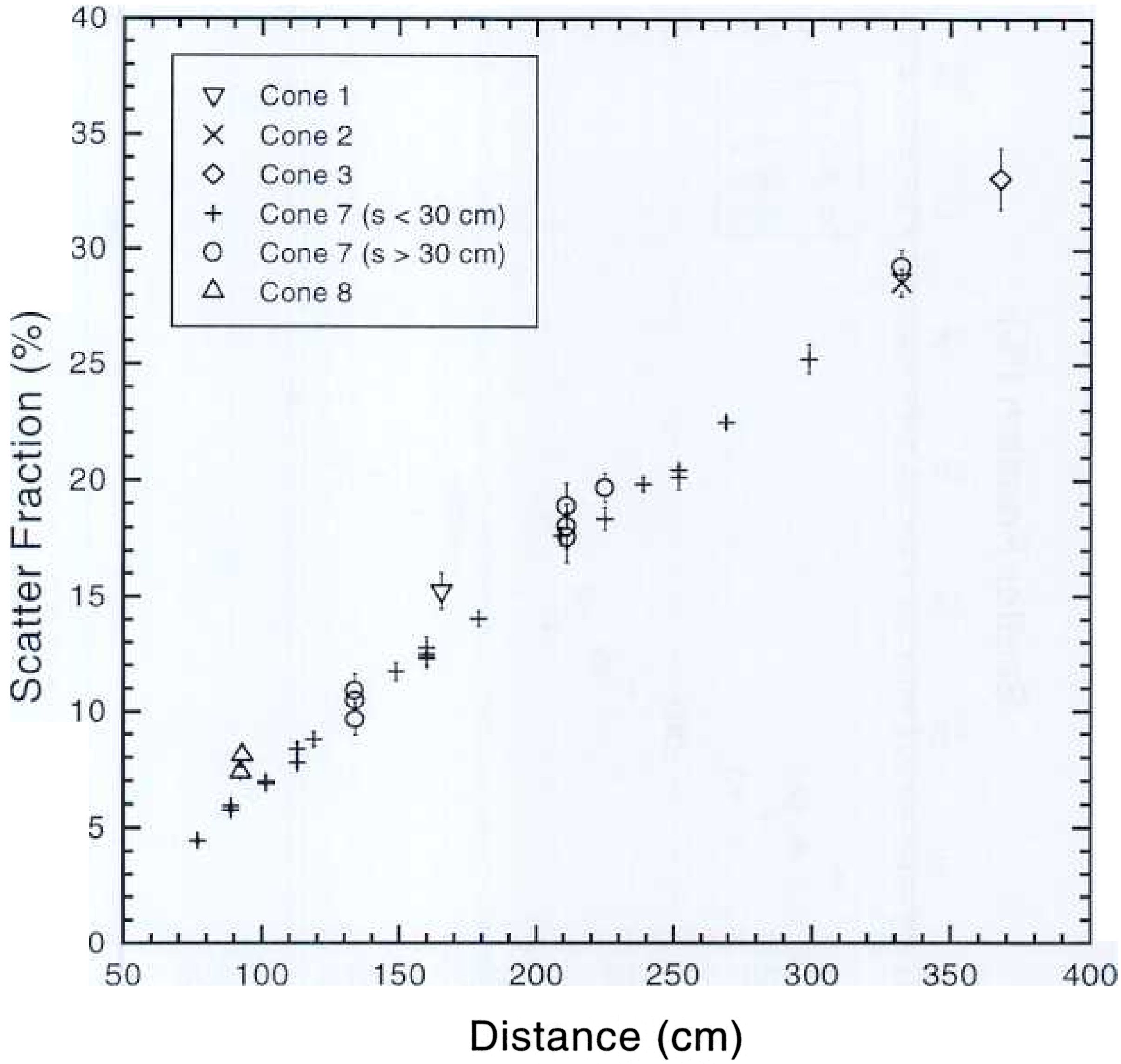

Figure 7. Effect of shadow cone number on scatter fraction. The data for cone #7, which has a 9 cm diameter narrow end, has been divided into two sets, grouped by the length of the source - cone separation (s).

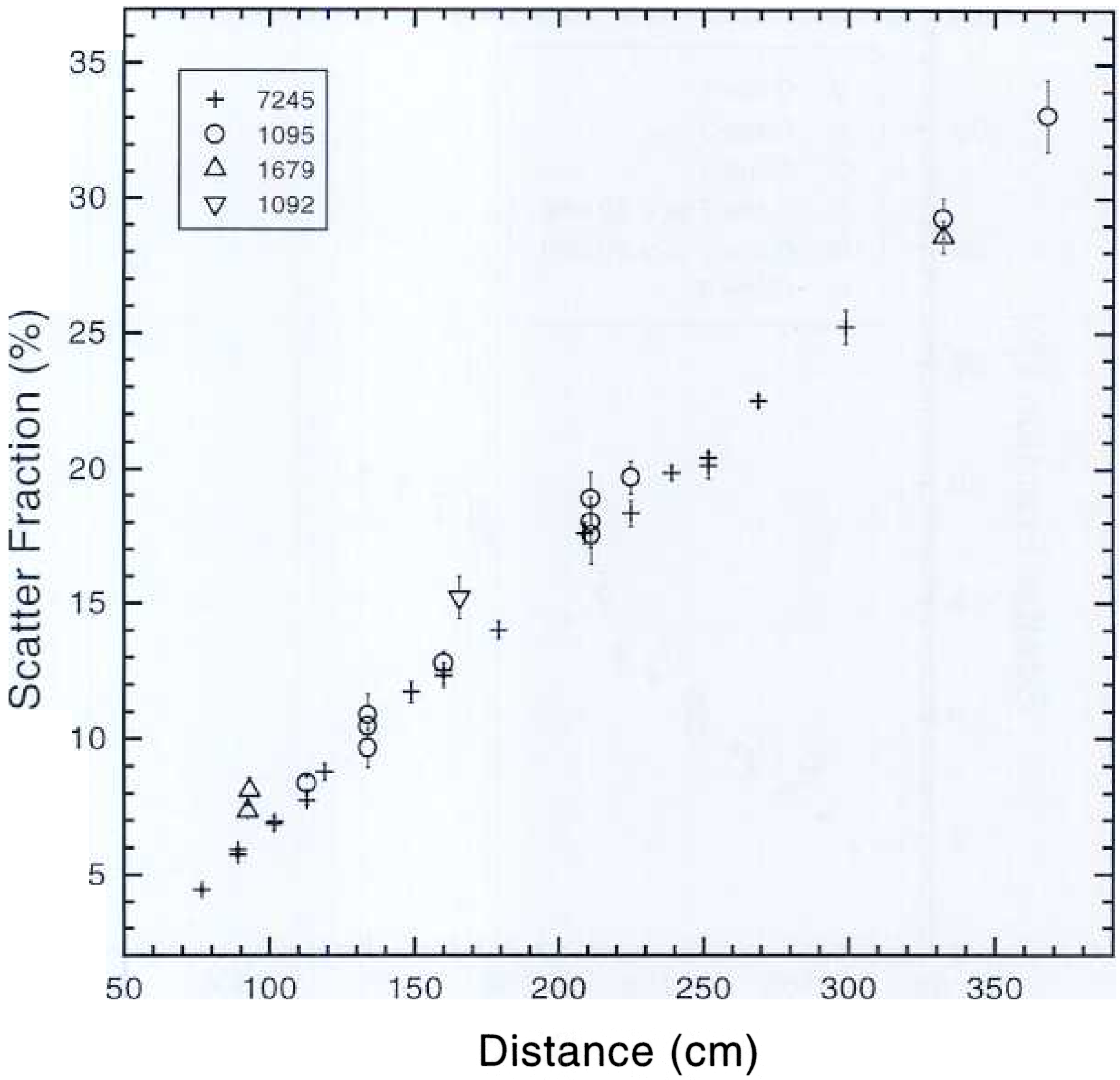

Figure 8. Effect of source number on scatter fraction. All sources have type X3 encapsulation, except for 7245 which has type X14 encapsulation.

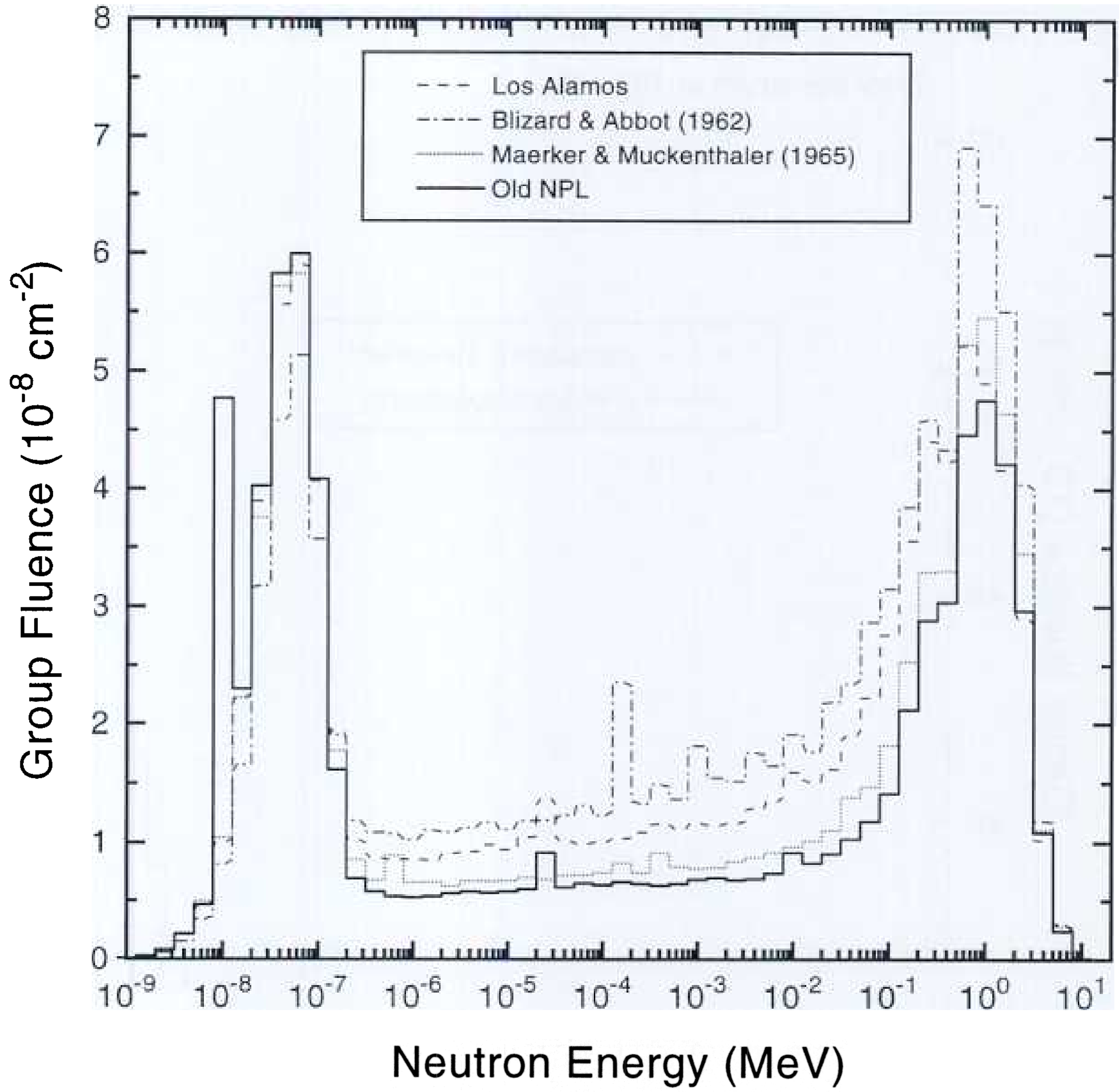

Figure 9. Effect of concrete composition on the total neutron spectrum 150 cm from a üCf source placed at the centre of a spherical concrete shell of inner diameter 1000 cm and outer diameter 1050 cm.

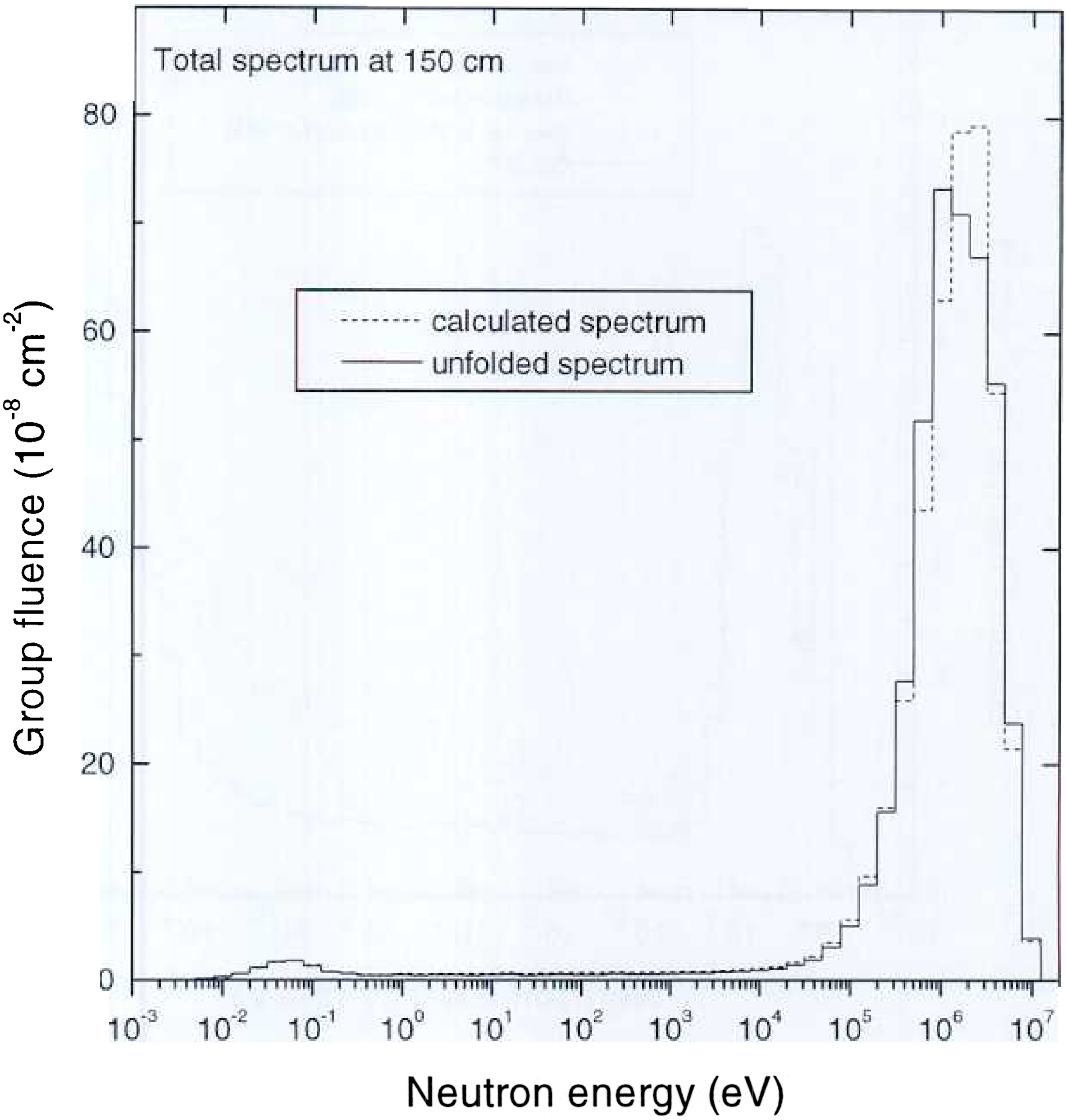

Figure 10. Comparison of MCNP calculated total fluence spectrum in the NPL low-scatter facility at 150 cm from a ^{252}Cf source with that unfolded from the Bonner sphere measurements using the calculation as the *a priori* guess spectrum for the unfolding.

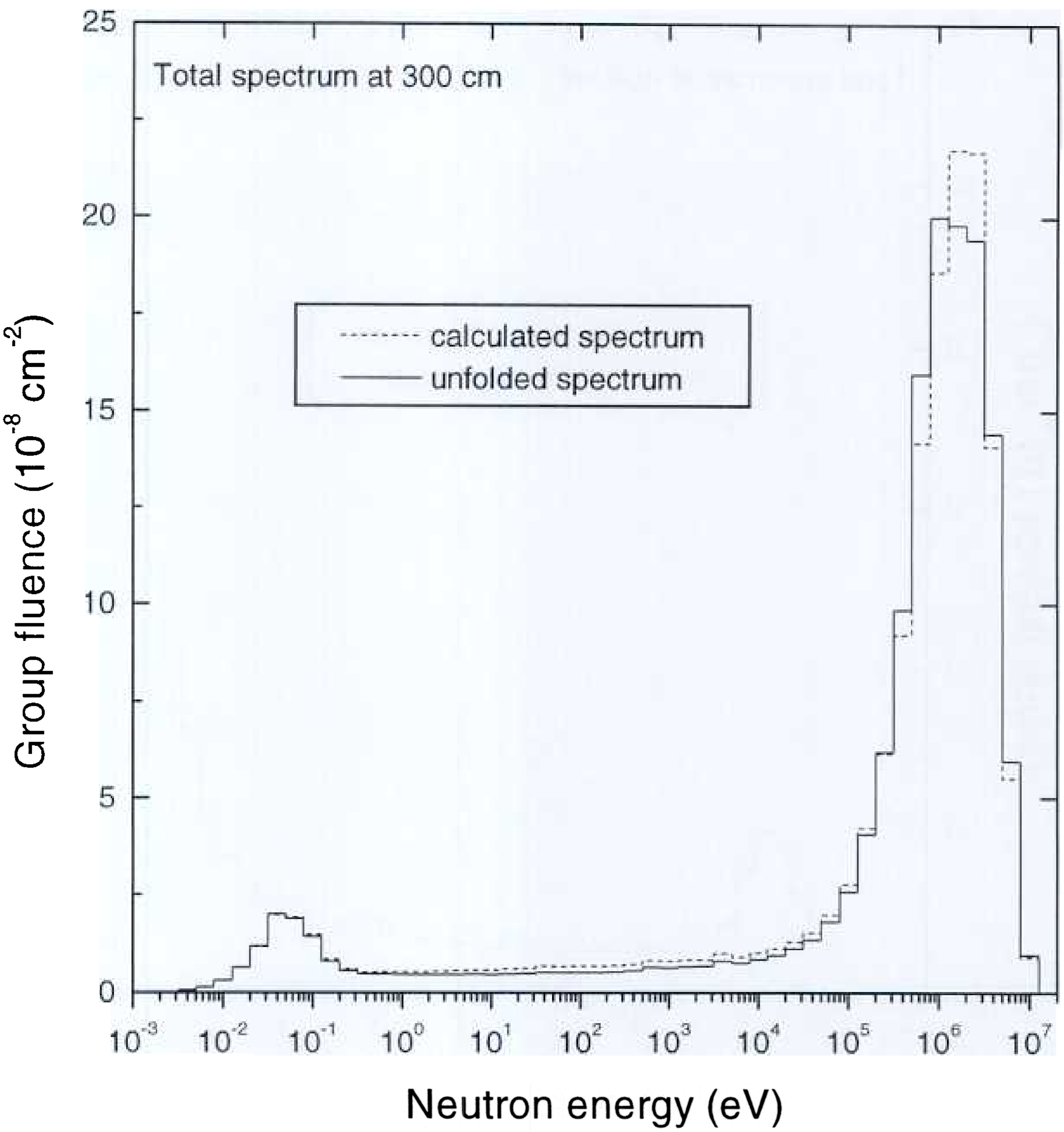

Figure 11. Comparison of MCNP calculated total fluence spectrum in the NPL low-scatter facility at 300 cm from a ^{252}Cf source with that unfolded from the Bonner sphere measurements using the calculation as the *a priori* guess spectrum for the unfolding.

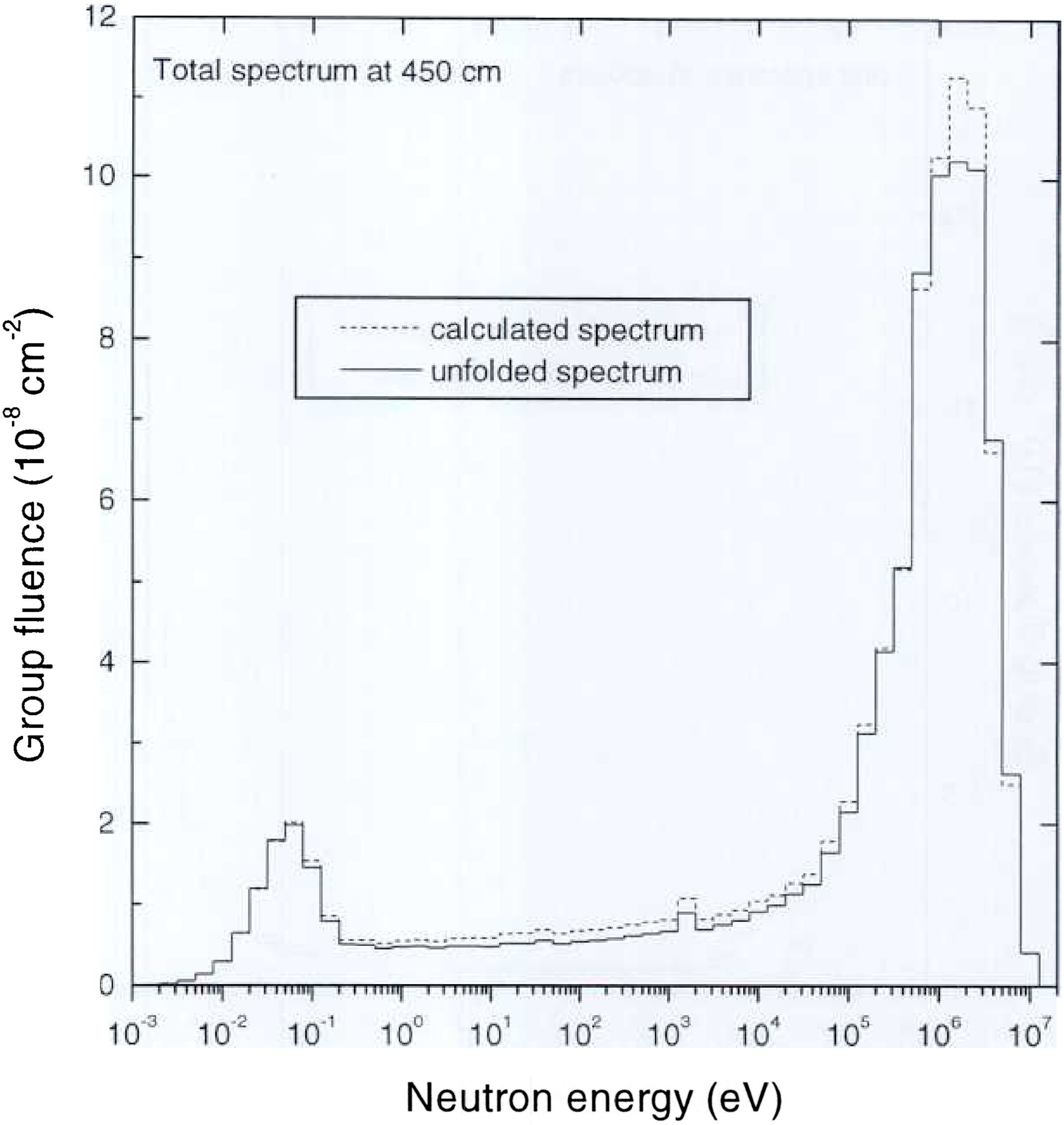

Figure 12. Comparison of MCNP calculated total fluence spectrum in the NPL low-scatter facility at 450 cm from a ^{252}Cf source with that unfolded from the Bonner sphere measurements using the calculation as the *a priori* guess spectrum for the unfolding.

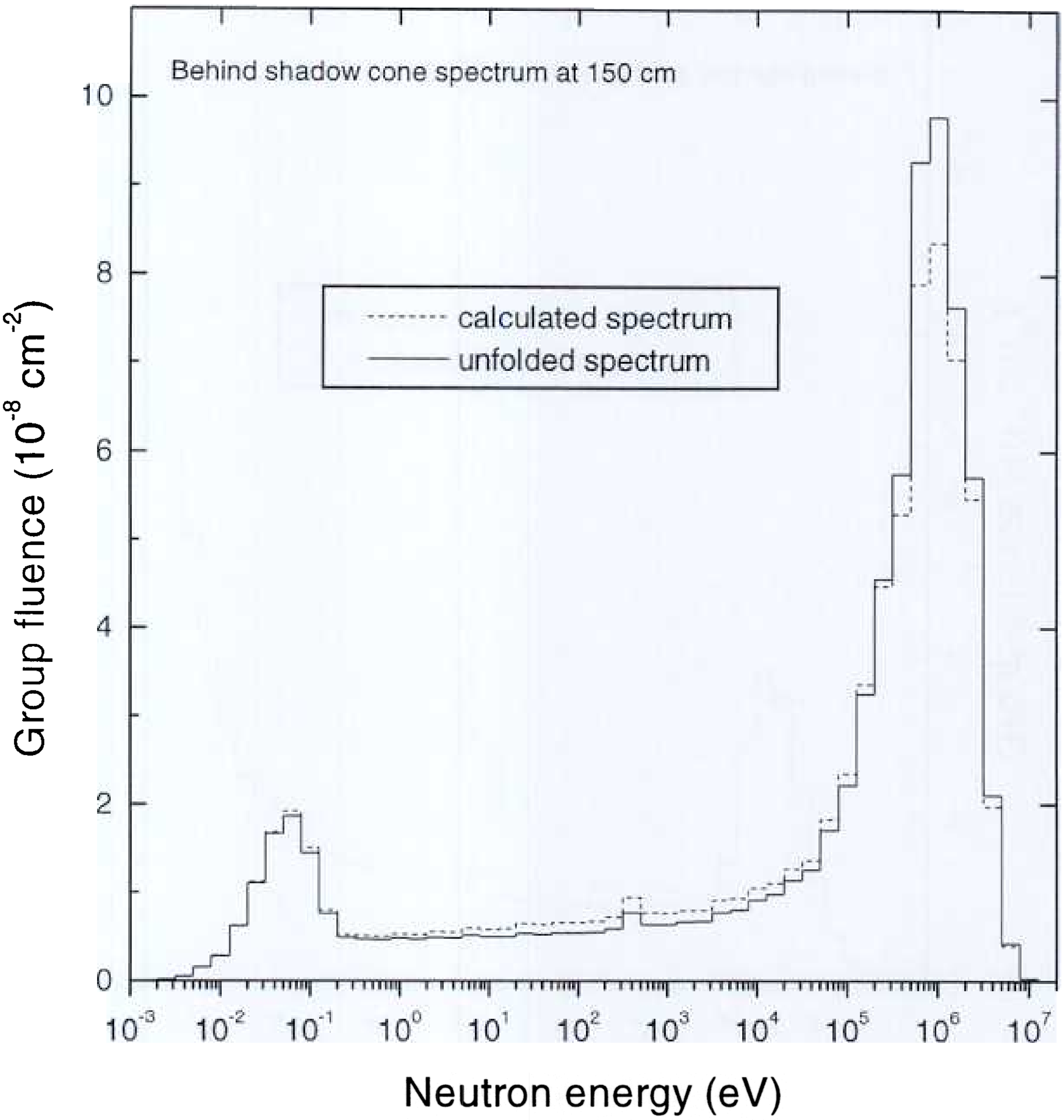

Figure 13. Comparison of MCNP calculated fluence spectrum behind a shadow cone in the NPL low-scatter facility at 150 cm from a ^{252}Cf source with that unfolded from the Bonner sphere measurements using the calculation as the *a priori* guess spectrum for the unfolding.

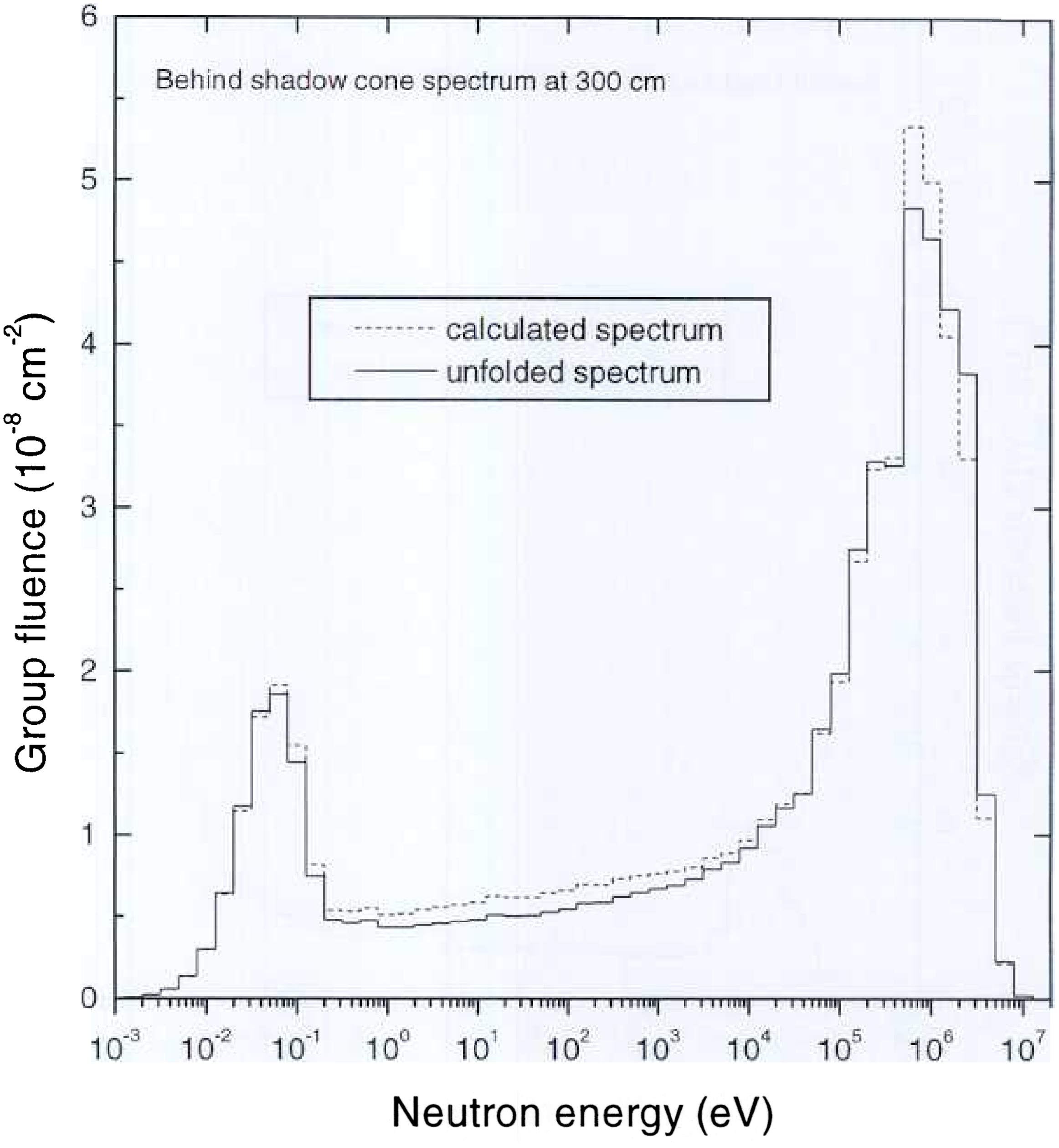

Figure 14. Comparison of MCNP calculated fluence spectrum behind a shadow cone in the NPL low-scatter facility at 300 cm from a ^{252}Cf source with that unfolded from the Bonner sphere measurements using the calculation as the *a priori* guess spectrum for the unfolding.

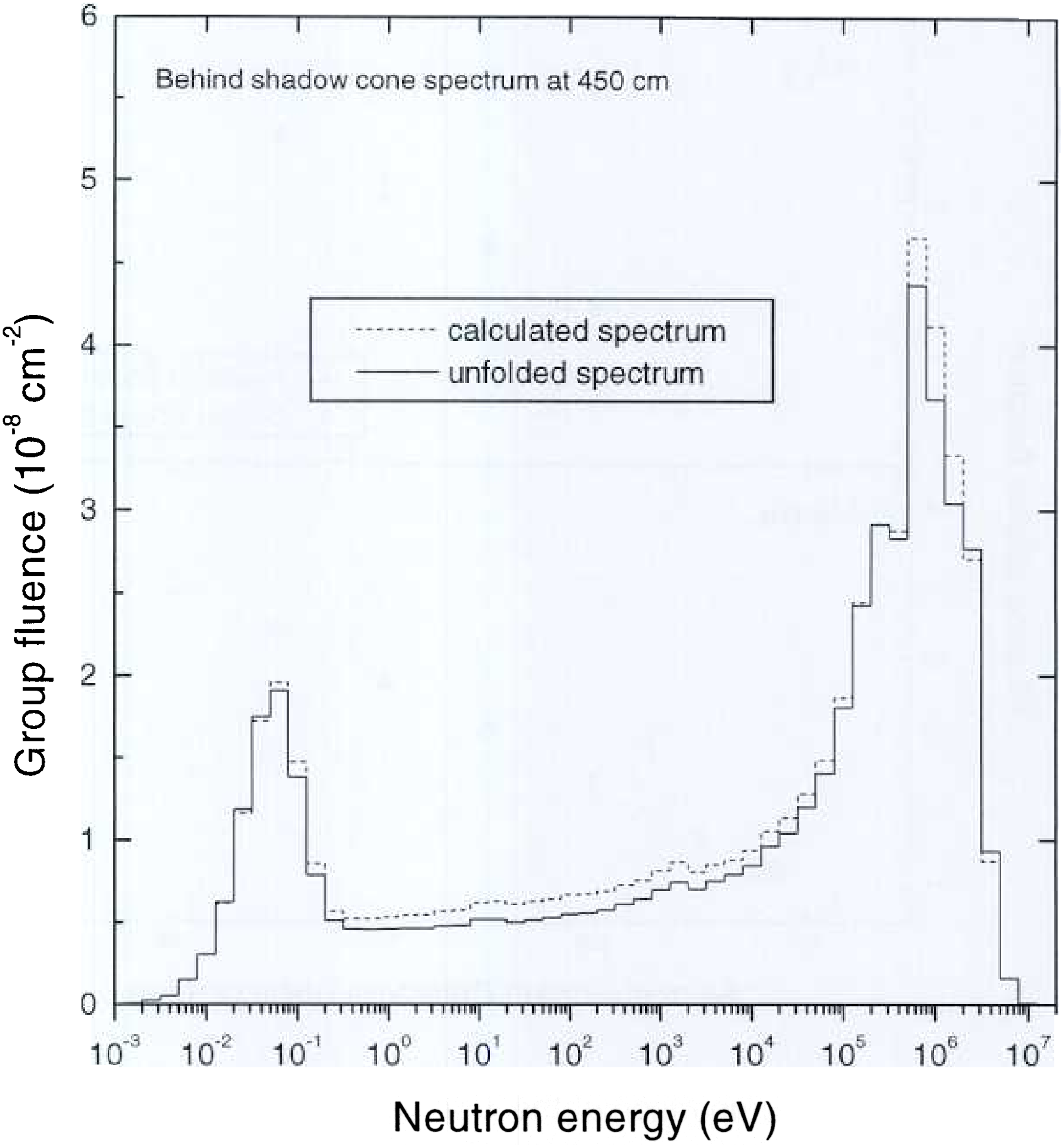

Figure 15. Comparison of MCNP calculated fluence spectrum behind a shadow cone in the NPL low-scatter facility at 450 cm from a ^{252}Cf source with that unfolded from the Bonner sphere measurements using the calculation as the *a priori* guess spectrum for the unfolding.

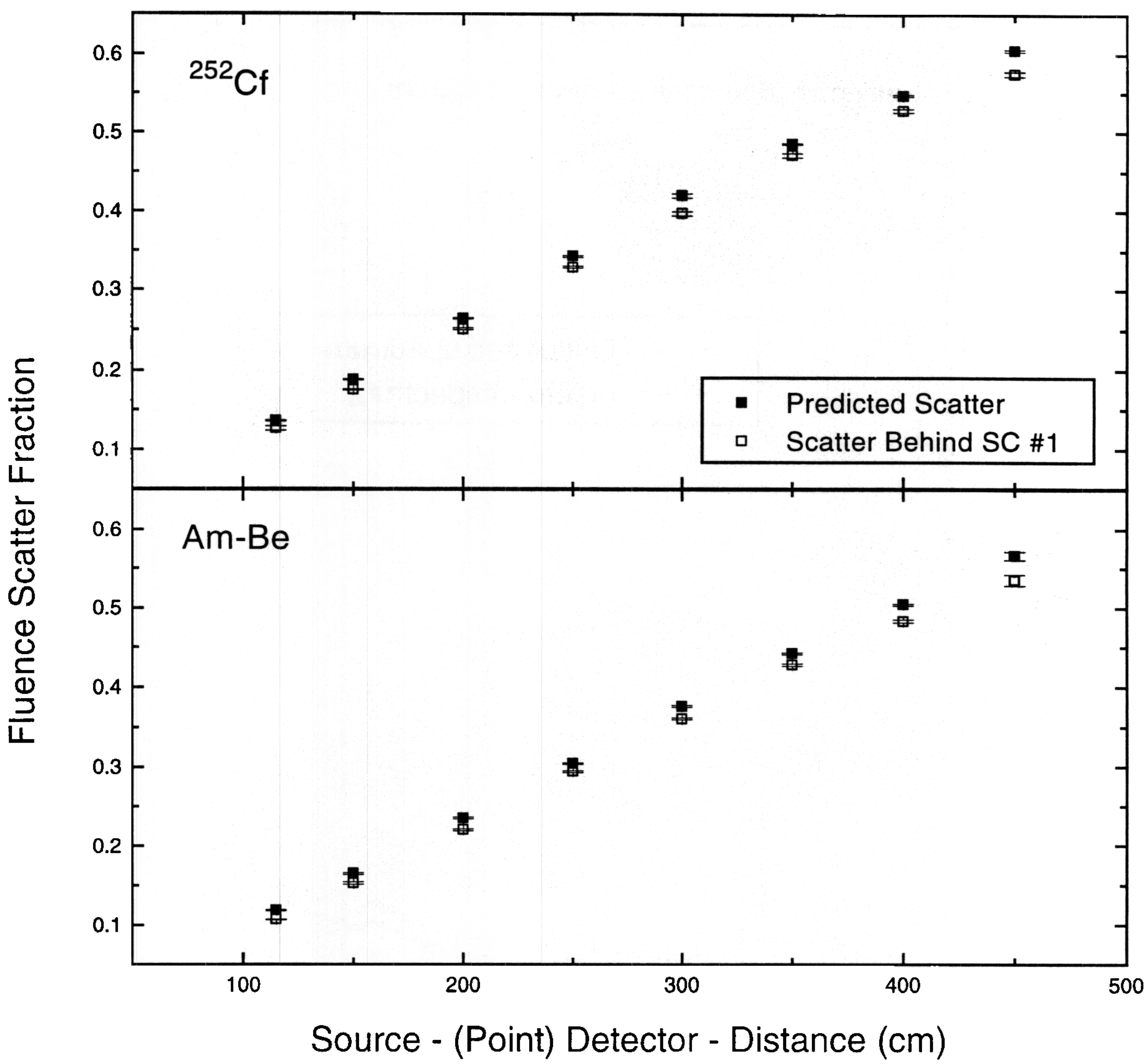

Figure 16. Comparison of the 'true' fluence scatter fraction, predicted using the series of models with no shadow cone, with the fluence scatter fraction predicted separately behind shadow cone #1. The comparison indicates that the shadow cone blocks a small component of the scatter as well as the neutron fluence directly from the source.

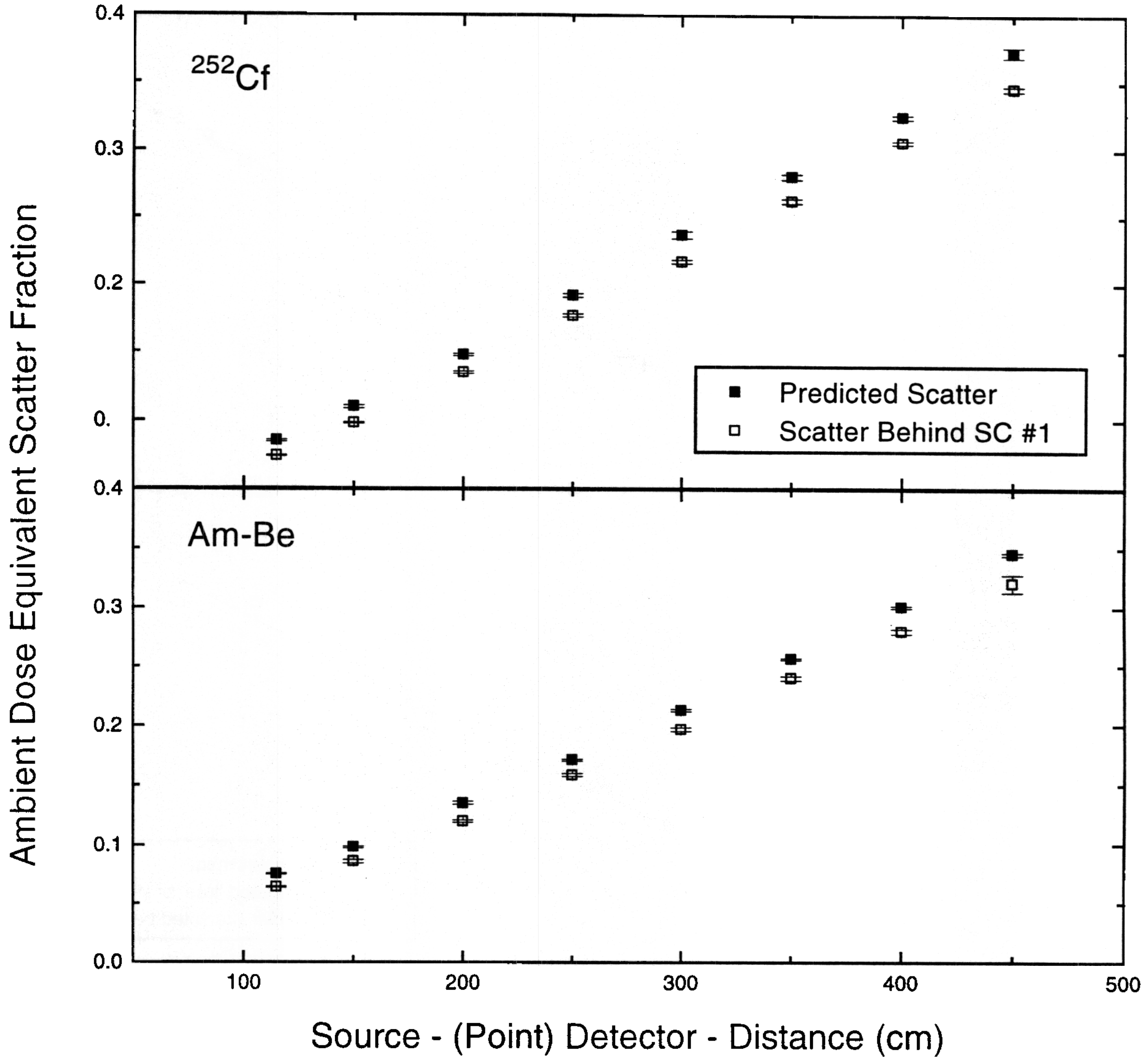

Figure 17. Comparison of the 'true' scatter fraction in terms of ambient dose equivalent ($H^*(10)$), predicted using the series of models with no shadow cone, with the scatter fraction in terms of dose equivalent predicted separately behind shadow cone #1. The comparison indicates that the shadow cone blocks a small component of the scatter as well as the neutron fluence directly from the source.

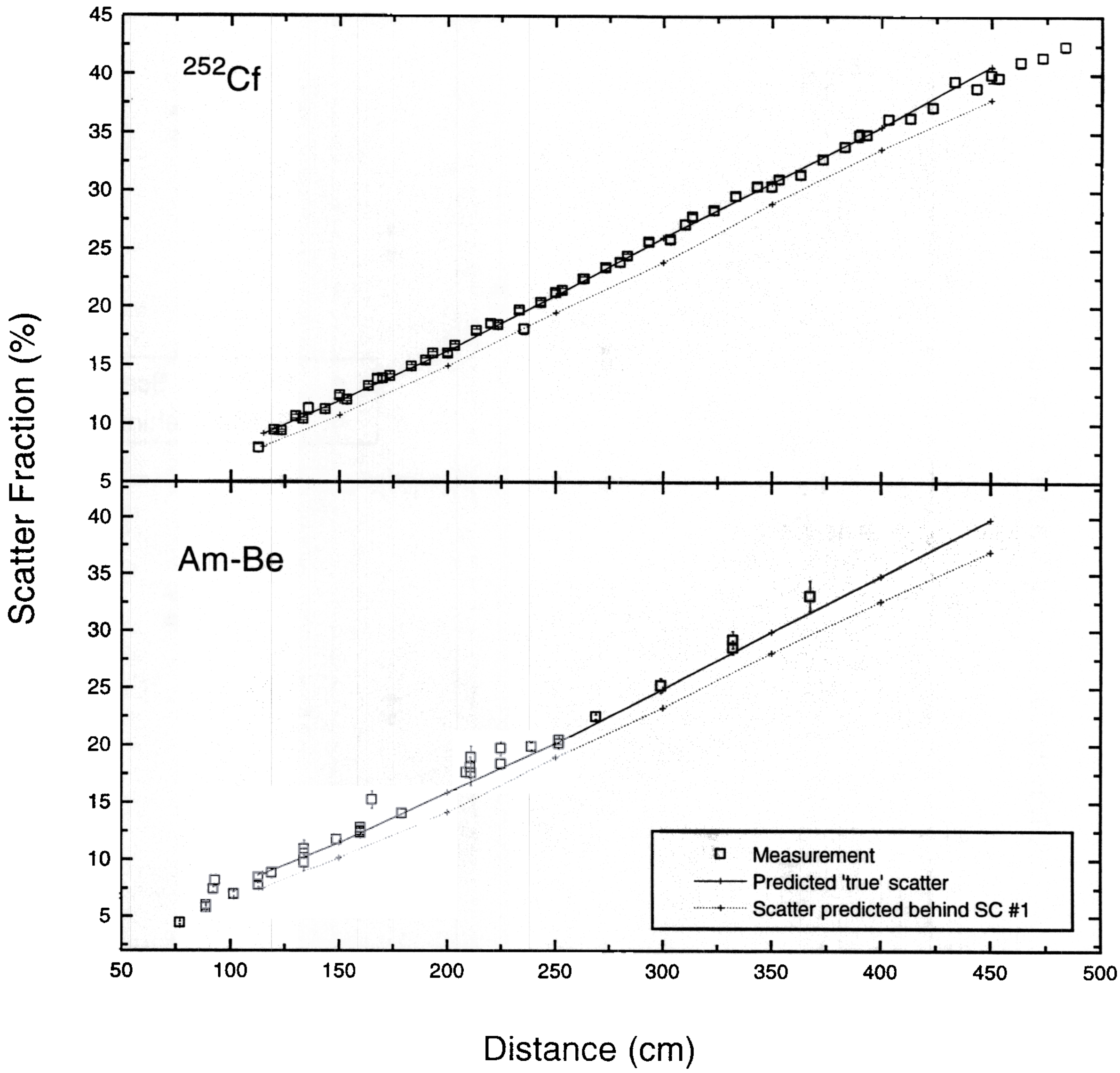

Figure 18. Comparison of the measured scatter fractions for the 0949 and Mk7 NRM instruments with predicted values calculated by folding the spectra predicted using MCNP with the response function data for the 0949 instrument.

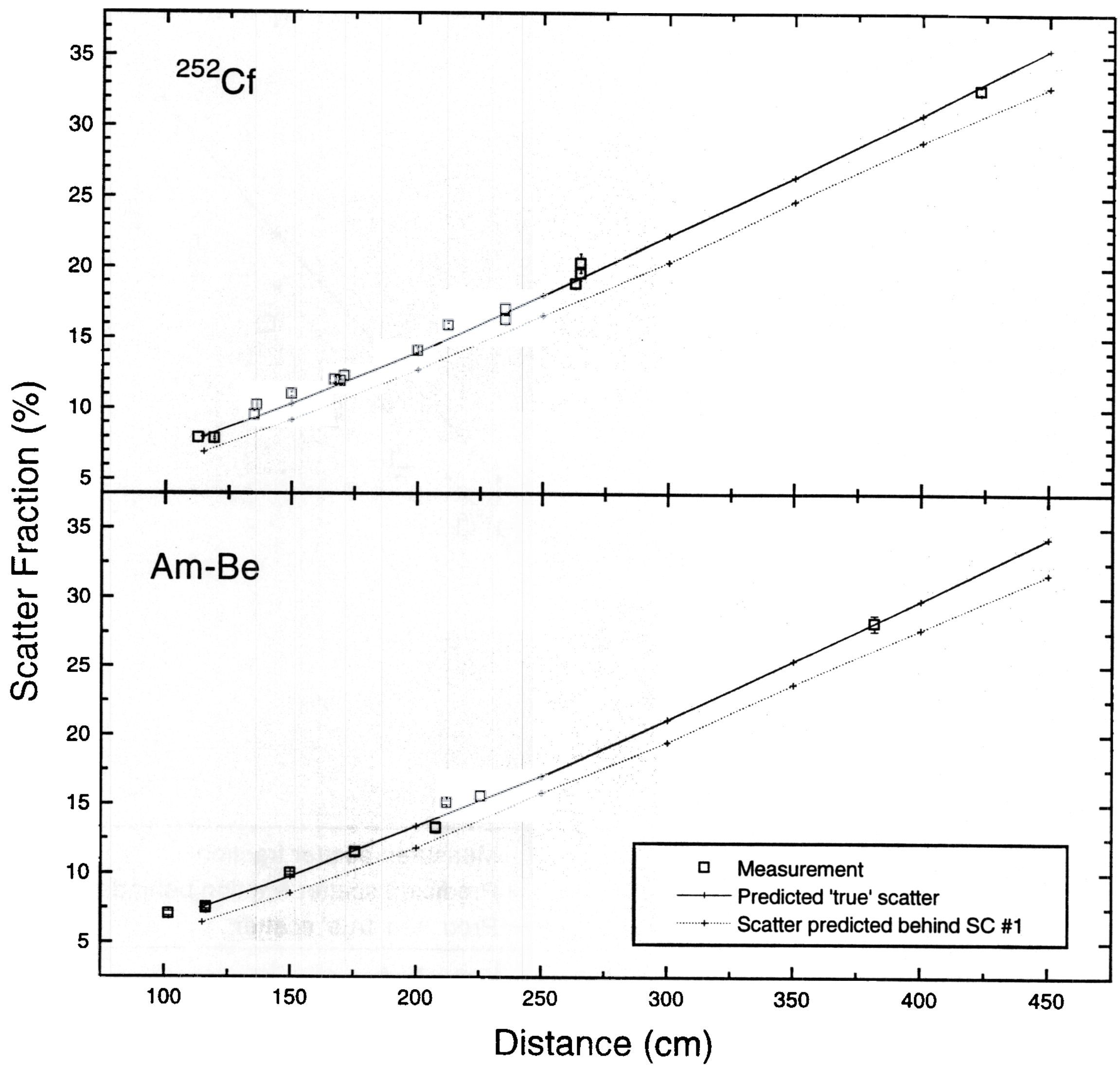

Figure 19. Comparison of the measured scatter fractions for the Studsvik 2022D instrument with predicted values calculated by folding the spectra predicted using MCNP with the response function data for the Studsvik instrument.

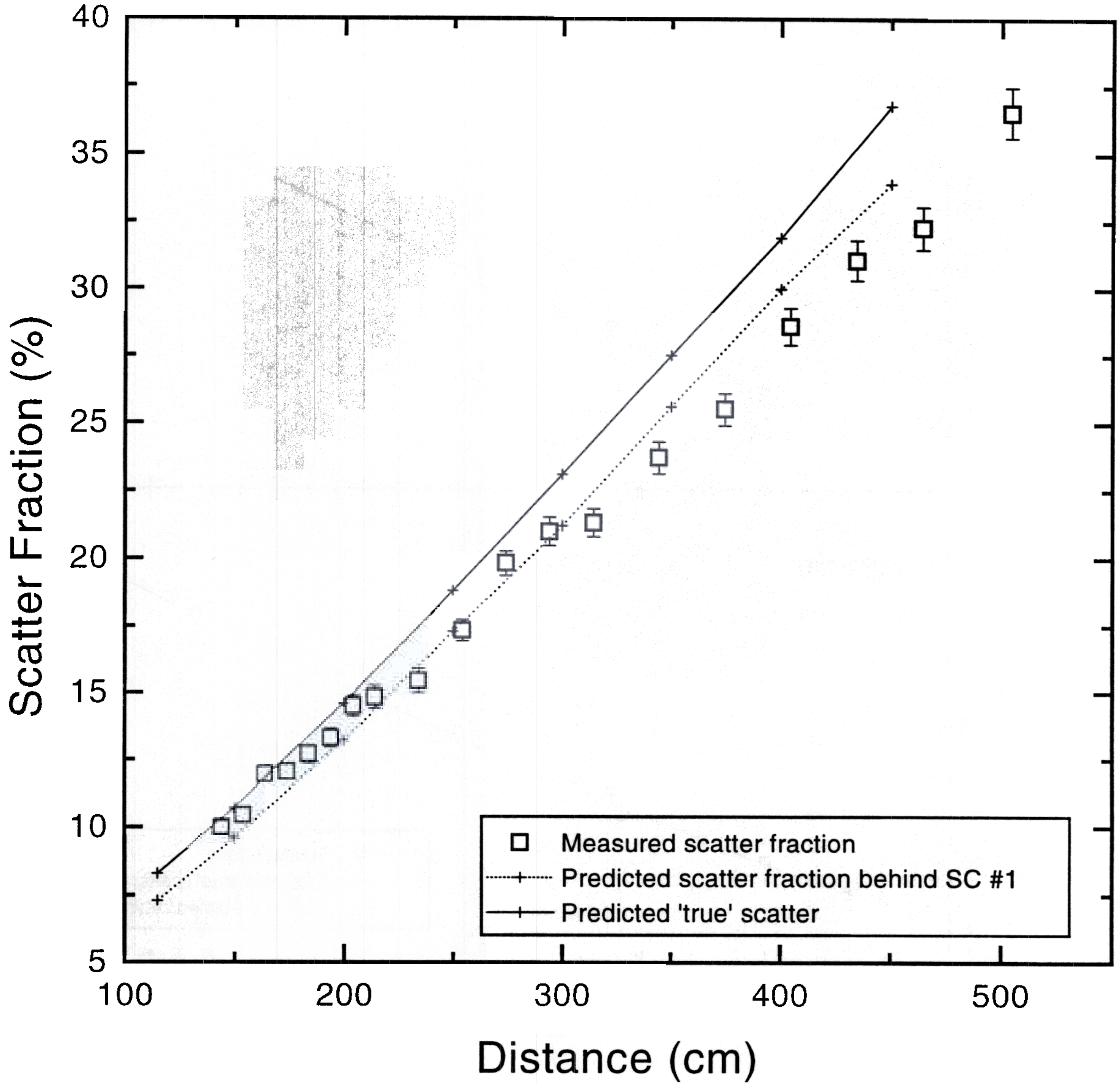

Figure 20. Comparison of the measured NM2 scatter fraction data with predictions derived by folding the calculated spectra with the NM2 response functions.